MODELED AND MEASURED PARTIALLY-COHERENT ILLUMINATION SPECKLE EFFECTS FROM SLOPED SURFACES FOR TACTICAL TRACKING

THESIS
MARCH 2015

Noah R. Van Zandt, Civilian, AD-21, USAF

AFIT-ENP-MS-15-M-257

DEPARTMENT OF THE AIR FORCE
AIR UNIVERSITY

AIR FORCE INSTITUTE OF TECHNOLOGY

Wright-Patterson Air Force Base, Ohio

AFIT-ENP-MS-15-M-257

MODELED AND MEASURED PARTIALLY-COHERENT ILLUMINATION SPECKLE EFFECTS FROM SLOPED SURFACES FOR TACTICAL TRACKING

THESIS

Presented to the Faculty

Department of Engineering Physics

Graduate School of Engineering and Management

Air Force Institute of Technology

Air University

Air Education and Training Command

In Partial Fulfillment of the Requirements for the

Degree of Master of Science in Optical Science and Engineering

Noah R. Van Zandt, BS

Civilian, AD-21, USAF

March 2015

AFIT-ENP-MS-15-M-257

MODELED AND MEASURED PARTIALLY-COHERENT ILLUMINATION SPECKLE EFFECTS FROM SLOPED SURFACES FOR TACTICAL TRACKING

Noah R. Van Zandt, BS
Civilian, AD-21, USAF

Committee Membership:

Steven T. Fiorino, PhD
Chairman

Jack E. McCrae, PhD
Member

Michael A. Marciniak, PhD
Member

Abstract

This work investigates the statistical properties of speckle relevant to short to medium range (tactical) active tracking engagements involving partially temporally coherent (polychromatic) illumination. A numerical model is developed to allow rapid simulation of speckled images including the speckle contrast reduction effects of illuminator bandwidth, surface slope and roughness, and the polarization properties of the source and surface. Regarding surface slope, Huntley's theory for speckle contrast, which employs geometrical approximations to decrease computation time, is modified to increase fidelity by incorporation of previously developed correction factors. A laboratory experiment is conducted to validate both the numerical model developed here and existing theory developed by Hu. A 671 nm diode laser source with coherence length of 259 +/- 7 μm is reflected off of a silver-coated diffuse surface. The reflections from diffraction-limited pixel viewing areas of 1.77 +/- 0.03 mm diameter are recorded via a CMOS detector array. The geometry is chosen such that speckles are well resolved with 4.8 +/- 0.1 pixels across each speckle width. The target surface is rotated about its normal between image captures to provide about 1,800 independent speckle samples for each slope angle, and data is gathered for 16 surface slope angles corresponding to speckle contrast between about 0.55 and 1. Data for polarization and surface roughness is also gathered and used to compare the theoretical and observed speckle contrasts. Taking Hu's theory as truth, the measurements show only -1.1% mean difference with 2.9%

standard deviation, while the modified Huntley equation has 1.4% mean difference with 1.0% standard deviation. Thus, good agreement between the measurements, Hu's theory, and the modified Huntley equation is found, and the theory is validated over the range of this experiment. Further, measured speckle size matches theory fairly well with some disagreements. Finally, measurements show that existing approximations for speckle irradiance PDF differ significantly from the physics, and better PDF models are needed.

Acknowledgments

I would like to thank my faculty advisor, Dr. Steve Fiorino, for his guidance throughout every stage of my thesis effort. I would also like to thank my other committee members, Drs. Jack McCrae and Mike Marciniak, for their insightful discussions and instruction. The experience and knowledge which I gained from each of these men is greatly appreciated. Also, I would like to thank the High Energy Laser Joint Technology Office for financial support of this research effort.

Noah R. Van Zandt

Table of Contents

Page

List of Figures

Page

List of Tables

Page

MODELED AND MEASURED PARTIALLY-COHERENT ILLUMINATION SPECKLE EFFECTS FROM SLOPED SURFACES FOR TACTICAL TRACKING

I. Introduction

This research investigates the statistics of speckle phenomena in the image plane for short to medium range (tactical) active tracking scenarios with a focus on high energy laser (HEL) tracking applications (See the List of Symbols, Abbreviations, and Acronyms after the Bibliography for a complete list of acronyms.). In particular, it addresses a partially temporally coherent (polychromatic) source illuminating an optically rough surface for coincident observation and incidence angles which are not necessarily normal to the surface. The speckle contrast is defined as a function of surface slope, illuminator coherence length, surface roughness, and polarization properties of the illuminator and surface. It is found that for many targets, surface slope dominates the speckle contrast. A method for numerically modeling speckle contrast is also developed. Additionally, the speckle statistics are compared to experimental results to validate the numerical models and their utility for target interrogation, aimpoint identification, and accurate modeling of active illumination tracking.

1.1 Background

With the advent of compact, high power solid-state lasers and new mission goals, such as counter-UAV (unmanned aerial vehicle) and counter-RAM (rockets, artillery, and mortars), the directed energy (DE) community has experienced a marked shift in focus to shorter-range missions than were typically considered in the past [Motes and Berdine, 2009; Butler, 2011; LaGrone, 2014; Boeing Defense, Space & Security, 2014]. Because high energy laser (HEL) weapons are capable of exceptional precision, their tracking requirements are typically very demanding even for shorter range tactical scenarios [Van Zandt et al., 2012]. To reduce tracking error, active illumination is often considered for a variety of reasons including increasing signal-to-noise ratio (SNR), increasing resolution over longer wavelength mid-wave infrared (MWIR) and long-wave infrared (LWIR) passive imaging, or eliminating dependence upon target emission and solar reflection.

Figure 1.1 shows one example of a situation in which active tracking outperforms passive, increasing the HEL system's keep-out-zone. Here, keep-out-zone is defined as the area about the HEL system in which targets can be engaged and destroyed quickly. In Figure 1.1, the green and yellow shaded regions indicate short kill times of a few seconds or less. The left and right plots differ only in illumination type, with passive and active illumination used respectively. Active illumination extends the yellow region of the keep-out-zone significantly, making the HEL more effective. While this figure represents only one scenario, it shows the type of HEL system performance increase which can result from active illumination.

However, active tracking has disadvantages, one of the primary disadvantages being the introduction of speckle phenomena, which is the focus of this work. Figure 1.2

shows an example of a speckled image of a distant target. The target is a 4 m wingspan UAV at 9 km altitude and 16 km slant range. The speckles are the bright and dark spots in the image caused by the combination of the partial coherence of the laser illuminator and the microscopic rough surface features of the target. Besides speckle, other active illumination disadvantages include increased system size, weight, and power requirements, increased complexity, and potentially lower SNR during the day, when solar irradiance can be hard to compete with. Because of these disadvantages, active illumination is not always the right answer, creating a need to understand the disadvantages of active illumination, including speckle.

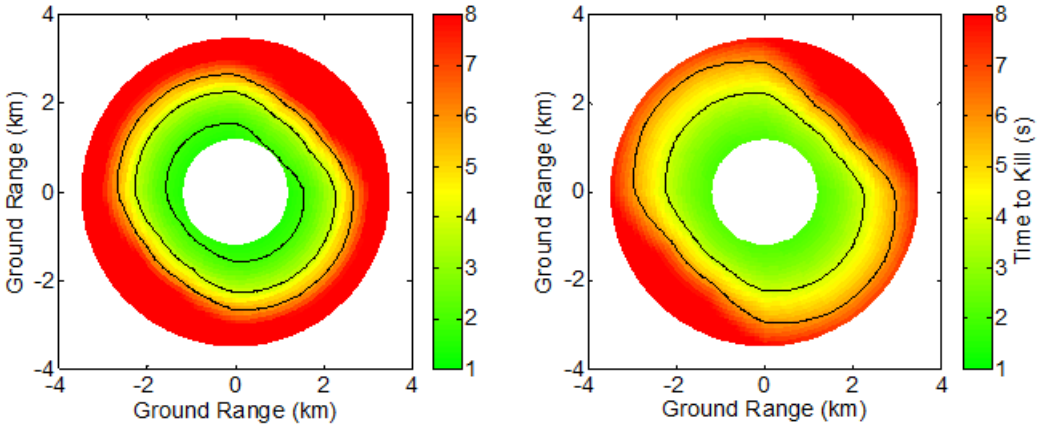

Figure 1.1. HEL keep-out-zone comparison of passive and active illumination. The left and right plots represent identical systems except that passive illumination and active illumination are used respectively. A target flying within the green and yellow regions can be disabled quickly. Performance is visibly increased with active illumination, mostly due to the increase in the yellow region. These plots were created using PITBUL for active tracking modeling and HELEEOS for HEL modeling. Conditions: 0.5 m wingspan UAV target at 100 m altitude flying directly toward the HEL, HEL at ground level, 50 w pulsed active illumination at 1.1 µm wavelength, 1.5 cm coherence length, and a passive tracking band of 3 µm to 5 µm.

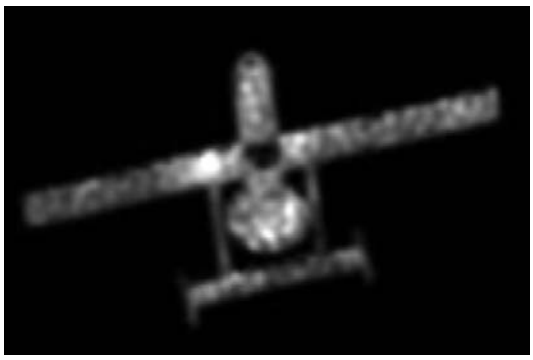

Figure 1.2. A speckled image of an actively illuminated UAV. The speckles are the bright and dark spots across the image. Partially developed speckle is shown here due to the short coherence length of the illuminator and sloped surfaces of the target. Conditions: 1.1 μm wavelength pulsed illuminator with 1.5 cm coherence length and 500 w average power, 4 m wingspan UAV at 9 km altitude and 16 km slant range.

While the implications of speckle phenomena have been well-defined for long range active tracking [Riker, 2011; Baribeau and Rioux, 1991], little published research exists regarding the statistics and impact of speckle for shorter range scenarios. Because of the exceptional tracking requirements of HEL systems, speckle effects need to be well understood in order to assess the utility of active illumination during the HEL system design process. Speckle effects are a function of many parameters including surface slope and roughness, illuminator coherence length, polarization properties of the illuminator and surface, atmospheric turbulence, and target motion. Furthermore, because speckle is a function of surface slope, the magnitude of the phenomena will vary over the spatial dimensions of a three-dimensional target, potentially introducing both detrimental and beneficial properties to the target imagery.

1.2 Applications

A proper understanding of speckle phenomena for tactical tracking scenarios has a number of applications including the numerical analysis of both active tracking performance and speckle-based measurement of surface slopes across the target. First, speckle theory for short range scenarios will find application in the analysis and numerical simulation of active tracking by providing a rigorous basis for estimates of tracking error. Potential uses in this area include comparison studies between active and passive illumination for system design and optimal selection of tracking loop bandwidth. Regarding tracking loop bandwidth, previous work has indicated that the optimal tracking bandwidth is the maximum possible bandwidth, which best compensates for target motion and turbulence effects [Riker, 2011]. However, for a dynamic target in the presence of speckle and turbulence, the speckle pattern changes over time as a function of both target and atmospheric motion. Because a speckled image averaged over many independent speckle realizations produces an unspeckled image, it is desirable to minimize the tracking bandwidth in order to average out the speckle. Thus, when speckle is included, the optimal tracking bandwidth can be lower than the maximum possible bandwidth.

The second class of applications for tactical speckle theory involves the measurement of target surface slope. Because speckle contrast is a strong function of surface slope as referenced to the illumination/imaging line of sight (LOS), it is possible to extract surface slope information from speckle imagery [Van Zandt, 2014]. Such information could find use for target identification. Additionally, certain target regions or aimpoints can also be identified from surface slope [Van Zandt, 2014]. One such

aimpoint is the wing joint of most aircraft, which is found at the junction of the wing and the fuselage, two areas which often have different surface slopes relative to the LOS. This concept will be discussed further in Section 5.2.

1.3 Thesis Outline

Chapter 2 examines the theory of speckle phenomena for tactical scenarios. Speckle statistics including irradiance distribution, size, and contrast are examined for an imaging geometry including the impacts of aperture size, illuminator characteristics, and surface properties. The experimental methodology and layout is covered in Chapter 3. Chapter 4 presents the experimental results with comparison to the numerical simulation results for model validation over the experimental range. A summary and concluding remarks are given in Chapter 5, along with proposals for future research.

II. Literature Review

Investigation of speckle phenomena began in earnest with the development of the first commercial lasers in the 1960s. Researchers working on the early lasers noticed that laser light which was reflected off of most common materials appeared to the human eye to be speckled or broken up into small bright and dark spots [Goodman, 2007:1]. They quickly attributed this speckle pattern to the random phasor sum which results from the detection of coherent (laser) light reflected off of an optically rough surface. It is important to note that most surfaces, even those which seem fairly smooth to the touch, are rough compared to optical wavelengths. The random surface roughness imparts a random phase pattern on the light which reflects off of that surface. When that light is collected and interfered during measurement, a random phasor sum results which causes a spatially random component in the detected irradiance pattern known as speckle.

Over the last fifty years, a wide breadth of research has been conducted into this phenomenon with application in fields from microscopy to laser range finding [Goodman, 2007]. In this section, the portion of that research relevant to the modeling of speckle for modern tactical active tracking is reviewed. First, statistical theory of fully developed speckle is derived, theory which assumes full coherence and complete polarization of both source and reflection. Next, statistical theory regarding reduction in speckle contrast is presented, including reduction due to polarization diversity, polychromatic light, surface roughness, and surface slope. Third, as reduction due to surface slope tends to dominate in most cases, a more complete physical optics theory for

that reduction factor is presented to provide a point of comparison with the simpler but broader model which is more commonly used.

2.1 Statistical Properties of Fully Developed Speckle

Rigorous solutions to speckle problems often require extensive inquiry into the propagation of electromagnetic waves and many have no known analytical form [Goodman, 2000:348; Hyde 2013; Huntley, 1999]. However, it is often sufficient to take a much simpler statistical approach involving random phasor sums. Such an approach for speckle with a fully coherent illuminator and fully polarized light is presented here both as a basis for more complex theory to follow and as an example of the statistical methods employed in speckle analysis. The random phasor sum is defined as

$$\mathbf{A} = A\exp(i\theta) = \frac{1}{\sqrt{N}}\sum_{n=1}^{N} a_n \exp(i\theta_n) \tag{1}$$

where N is the number of phasors, and the nth phasor has length $a_n/\sqrt{N}$ and phase θ_n [Goodman, 2007:7]. Each phasor in the sum represents the complex electric field due to reflection from a single rough surface feature within the viewing area of the detector element, or instantaneous field of view (IFOV). The factor of $1/\sqrt{N}$ is added so that the sum converges as N is allowed to go to infinity.

Before progressing, four key assumptions are made. First, it is assumed that all phasor amplitudes and phases are statistically independent of all others. In other words, each rough surface feature's reflection is assumed to be independent of all other reflections. Second, all phasors share a common amplitude distribution with a known mean and variance, implying that the illumination is uniform over the pixel viewing area.

Conveniently, the mean can easily be found from radiometry under the assumption of incoherence. Also, because the central limit theorem will be used, the specific statistical distribution of amplitude is irrelevant. Third, assume that each detector element views a large number of independent rough surface features, which will allow the use of the central limit theorem and other approximations. Finally, assume the condition known as "fully developed speckle" by assuming that the wrapped phases are uniformly distributed over $(0, 2\pi)$ [Goodman, 2007:28]. This last assumption is justified as long as the surface height standard deviation is at least three times greater than the wavelength [Goodman, 2007:73], a condition which is almost always satisfied for tactical active tracking. As an example, a study by Boeing showed that the average surface roughness of a coated 737 aircraft body is about 3 μm in spite of considerable effort to reduce it in order to reduce aerodynamic drag [Boeing, 1983], while illuminator wavelengths are typically around 1 μm [St. Pierre, 1997; Post, 2004].

Next, break the random phasor sum down into real and imaginary components, *r* and *i*, as

$$r = \mathrm{Re}\{\mathbf{A}\} = \frac{1}{\sqrt{N}} \sum_{n=1}^{N} a_n \cos(\theta_n) \tag{2}$$

$$i = \mathrm{Im}\{\mathbf{A}\} = \frac{1}{\sqrt{N}} \sum_{n=1}^{N} a_n \sin(\theta_n) \tag{3}$$

By the central limit theorem, each component is approximately normally distributed. Further, by using the assumptions defined previously, it is not hard to show that the means of both *r* and *i* are zero, the correlation between the two is also zero, and the variance σ^2 of each is given by

$$\sigma^2 = \frac{< a^2 >}{2} \tag{4}$$

Thus, the joint probability density function (PDF) is

$$p_{RI}(r,i) = \frac{1}{2\pi\sigma^2}\exp\left(-\frac{r^2+i^2}{2\sigma^2}\right) \tag{5}$$

At this point, a transformation of variables yields the joint probability density function of the amplitude and phase of the random phasor sum according to

$$p_{A\theta}(A,\theta) = p_{RI}\left(A\cos(\theta), A\sin(\theta)\right) * \|J\| \tag{6}$$

where $\|J\|$ is the Jacobian of the transformation of variables. The resulting joint PDF is

$$p_{A\theta}(A,\theta) = \frac{A}{2\pi\sigma^2}\exp\left(-\frac{A^2}{2\sigma^2}\right) \tag{7}$$

Of particular interest is the marginal PDF of the amplitude $p_A(A)$, which is found by integration over θ yielding

$$p_A(A) = \frac{A}{\sigma^2}\exp\left(-\frac{A^2}{2\sigma^2}\right) \tag{8}$$

which is a Rayleigh density function. Alternately, the marginal PDF of the phase is found by integrating over the amplitude and is uniformly distributed over (0, 2π). Thus, the joint PDF is factorable into the marginal PDFs, and the amplitude and phase of the random phasor sum are independent [Goodman, 2007:7-13].

While these results are interesting, most optical detectors measure irradiance, *I*, not amplitude or phase. Thus, it is necessary to use another transformation of variables. Ignoring scaling constants, $I = A^2$. By using the same process as previously,

$$p_I(I) = p_A(A(I))\|J\| = \frac{1}{2\sigma^2}\exp\left(-\frac{I}{2\sigma^2}\right) \tag{9}$$

which is a negative exponential PDF. Speckle characterized by this PDF is often referred to as "fully developed speckle" [Goodman, 2007:28]. The mean irradiance is easily calculated as $< I >= 2\sigma^2$. Further, the standard deviation is $\sigma_I = 2\sigma^2$, equal to the mean.

Speckle contrast is a measure of the strength of the speckle effect and is defined as

$$C = \frac{\sigma_I}{< I >} \tag{10}$$

which the reader may recognize as the inverse of the standard optical definition of SNR. From this definition, the speckle contrast for fully developed speckle is unity. In general, speckle contrast will be reduced from unity by a number of speckle reduction factors to be discussed next.

2.2 Speckle Contrast Reduction

A number of factors can reduce speckle contrast. For tactical active tracking, the relevant factors are polarization diversity, surface roughness, and surface slope. Polarization diversity was investigated by early researchers, often in combination with other effects [Goodman, 2000:248-250]. The other two factors both involve source bandwidth and surface properties. The impact of surface roughness for polychromatic (finite coherence length) illumination was investigated both experimentally and theoretically in the 70s [Sprague, 1972; Pedersen, 1975a; Nakagawa and Asakura, 1979]. Also during that timeframe, the effects of geometry on polychromatic speckle for non-

imaging systems were investigated by Pederson and Parry [Pedersen, 1975b; Parry, 1975]. McKechnie extended the theory to imaging systems around the same time [McKechnie, 1976]. Almost twenty years later, Hu derived an expression for polychromatic speckle contrast which allowed for any imaging and illumination geometry except those involving near glancing angles with the surface [Hu, 1994]. The recent work involved experimentation, application, and engineering simplification of this theory [Huntley, 1999; Rodrigues and Pinto, 2003; Markhvida et al., 2007; Tchvialeva et al., 2008; Tchvialeva et al., 2011].

The first factor, polarization diversity, can reduce speckle contrast by up to a factor of two. Under polarized illumination, the rough surface may have the effect of separating the reflected light into the two linear polarization states, each of which can produce an independent speckle field. If the illuminator is unpolarized, then two independent speckle fields can form from each of the two illuminator polarizations [Goodman, 2007:142-143]. However, this condition is unlikely in active tracking, as most illumination lasers are nearly fully polarized [St. Pierre, 1997; Post, 2004]. For arbitrary polarization diversity, a commonly-used approximation is to reduce the contrast according to

$$C = \sqrt{\left(1 + P^2\right)/2} \tag{11}$$

where P is the degree of polarization [Goodman, 2007:49]. Allowing for both partial source polarization, P_s, and partial reflection polarization, P_r, the speckle contrast for polarization diversity is

$$C = \tfrac{1}{2}\sqrt{\left(1 + P_s^2\right)\left(1 + P_r^2\right)} \tag{12}$$

Thus, while polarization diversity can reduce speckle contrast by up to a factor of 2 (from four independent speckle fields), the probable case for active tracking is a reduction by $\sqrt{2}$ or less.

The next factor, surface roughness, is also generally small, producing $C \approx 1$ for typical tactical active tracking conditions. Under the assumptions of Gaussian source spectrum and surface height distribution, and after a good bit of math, Goodman shows that speckle contrast for the surface reflection case is given by

$$C = \left[1 + 2\pi^2 \left(\frac{\Delta\lambda}{\lambda_0} \right)^2 \left(\frac{\sigma_h}{\lambda_0} \right)^2 \left(\cos(\theta_{ill}) + \cos(\theta_{im}) \right)^2 \right]^{(-1/4)} \tag{13}$$

where $\Delta\lambda$ is the full 1/e spectral width of the source, λ_0 is the mean wavelength, σ_h is the standard deviation of the surface heights, θ_{ill} is the angle between the surface normal and the incident illumination, and θ_{im} is the angle between surface normal and imaging LOS [Goodman, 2007:176]. For the specific case of active tracking, the equation can be simplified slightly with $\theta_{ill} \approx \theta_{im}$, which yields

$$C = \left[1 + 8\pi^2 \left(\frac{\Delta\lambda}{\lambda_0} \right)^2 \left(\frac{\sigma_h}{\lambda_0} \right)^2 \cos^2(\theta_{ill}) \right]^{(-1/4)} \tag{14}$$

This equation can be plotted for extreme parameters. First, the coherence length for modern pulsed illumination lasers is typically in the range of 0.1 to 3 cm [St. Pierre, 1997; Post, 2004] (for a more detailed discussion, see [High Energy Laser Joint Technology Office, 2013]). Assume a worst-case (highest contrast reduction) of 1 mm coherence length at 1 μm wavelength. Using the typical coherence conversion ($\Delta\nu \approx c/l_c$

), this yields $\frac{\Delta\lambda}{\lambda_0} = \frac{\Delta v}{v_0} = \frac{3e11}{3e14} = 0.001$. Coherence reduction clearly increases with increasing σ_h, so assume a value of 400 μm. For reference, one heavily rusted rolled homogeneous armor (RHA) plate had measured σ_h of 383 μm [Stanton et al., 2005]. For such conditions, the speckle contrast as a function of LOS angle is shown in Figure 2.1. Even for this extreme case, contrast is reduced by less than a factor of 2 at most. Note that speckle contrast actually increases with increasing slope angle due to reduced apparent surface roughness. From this result, it is clear that speckle contrast is not greatly reduced by surface roughness.

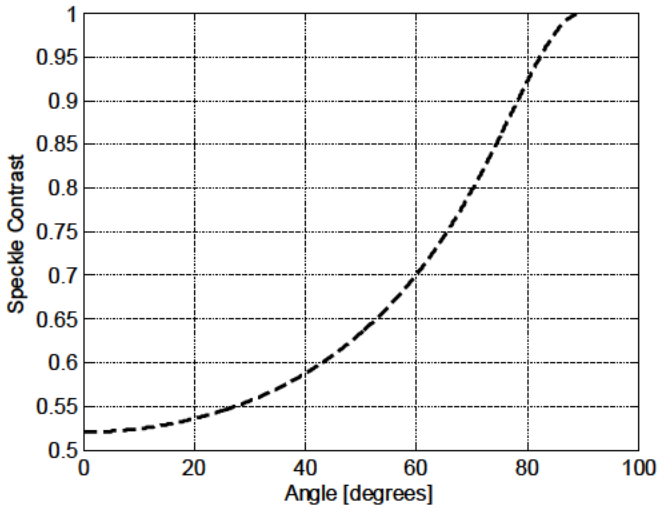

Figure 2.1. Speckle contrast for a "worst-case" (highest contrast reduction) scenario with 1 mm coherence length, 1 μm wavelength, and 400 μm surface height standard deviation. Speckle contrast never falls below one half.

One reduction factor has not yet been considered, surface slope, sometimes referred to as "geometry" or "illuminator and image directions." An analytical expression for speckle contrast given an arbitrarily sloped surface under partially coherent illumination was first developed by Hu [Hu, 1994]. Hu assumed Gaussian surface height distribution. A closed-form solution has not been found, but rather the equation is left in integral form,

$$C^2(\theta_{im},\theta_{ill}) = \left[1\Big/\int\int_{-\infty}^{\infty} S(\lambda)\,d\lambda\right]^2 \int\int_{-\infty}^{\infty} d\lambda_1 d\lambda_2 S(\lambda_1) S(\lambda_2) \exp\left(-4\pi^2\sigma^2\left(\cos(\theta_{im})+\cos(\theta_{ill})\right)^2\left(1/\lambda_2 - 1/\lambda_1\right)^2\right)$$

$$\times \frac{\left|\int\int_{-\infty}^{\infty} H\left(\lambda_1 R\left(x - \frac{\sin(\theta_{ill})}{\lambda_1\cos(\theta_{im})}\right), \lambda_1 Ry\right) H^*\left(\lambda_2 R\left(x - \frac{\sin(\theta_{ill})}{\lambda_2\cos(\theta_{im})} - \frac{\tan(\theta_{im})}{\lambda_1} + \frac{\tan(\theta_{im})}{\lambda_2}\right), \lambda_2 Ry\right) dxdy\right|^2}{\int\int_{-\infty}^{\infty}\left|H(\lambda_1 Rx, \lambda_1 Ry)\right|^2 dxdy \int\int_{-\infty}^{\infty}\left|H(\lambda_2 Rx, \lambda_2 Ry)\right|^2 dxdy} \quad (15)$$

where $S(\lambda)$ is the source spectral distribution, R is the target to aperture distance, σ is the surface height standard deviation, θ_{ill} is the angle between the surface normal and the illumination vector, θ_{im} is the angle between the surface normal and the imaging vector (with the opposite sign convention as θ_{ill}), $x = x'/\lambda R$, $y = y'/\lambda R$, x and y are the pupil plane spatial coordinates, and H is the pupil function [Hu, 1994]. To arrive at this equation for speckle contrast, Hu first found the point spread function (PSF) for a sloped surface target. Next, he computed the image-plane complex amplitude and its cross-correlation, accounting for surface roughness and arbitrary illumination angle. By assuming a Gaussian distribution of surface height and solving for the image-plane irradiance autocorrelation, the speckle contrast equation followed directly. This equation uses relatively few approximations and is based on physical optics, but it is not directly suitable for numerical simulation of active imaging, as its integral form requires

considerable computation time. However, it is still useful as a point of comparison with the computationally efficient equation discussed next, and it will be taken as truth moving forward.

Because of the computation time required to solve Hu's integral equation, Huntley developed a simplified model for engineering applications in 1999 [Huntley, 1999]. Huntley's key equation defines the number of independent coherence regions seen by each pixel based on geometrical approximations as

$$N = 1 + \frac{2r\sin\left(\psi + h/\rho\right)}{l_c} \tag{16}$$

where $r = \sqrt{\rho^2 + h^2}$, $\rho = \alpha s$, α is a scaling constant of order unity, $s = 1.22\lambda R/D$, R is the distance between object and aperture, $h = \beta\sigma$, β is a scaling constant of order unity, σ is the surface height standard deviation, ψ is the angle between the surface normal and the bisector of the illumination and observation rays, and l_c is the source coherence length. Huntley also used the common approximation for speckle contrast given N ,

$$C \approx \frac{1}{\sqrt{N}} \tag{17}$$

Further, Huntley's values for α and β are based on a curve fit of his equation to Hu's over a wide range of possible conditions.

Although the curve fit of Huntley's equation to Hu's shows relatively low error, it accounts for surface roughness, which is accounted for separately in this work by using the more exact expression presented previously. Also, it does not utilize the theoretically-

grounded corrections which have been developed to allow one to use geometrical approximations with little error (no error for certain well-bounded problems) [Goodman, 2000:242; Bures et al., 1972]. An expression for N fundamentally linked to Huntley's derivation but avoiding the two pitfalls just mentioned is

$$N = 2\tan(\theta)\frac{\alpha\lambda R}{Dl_c} \tag{18}$$

where θ is the angle between the coaxial illumination and imaging directions and the surface normal, α is a scaling constant of order unity (the IFOV coefficient), D is the imaging aperture diameter, and l_c is the illuminator coherence length. This equation should be thought of as simply the number of coherence areas on target seen by each pixel. The leading factor of two accounts for the two-pass reflection of light approaching the surface from the imaging direction. Thus, $2\tan(\theta)\alpha\lambda R/D$ is the effective surface depth, and the division by l_c breaks the depth up into coherence areas caused by surface slope. From curve fits to the more exact Hu equation, the IFOV coefficient α is 1.749 for either a Gaussian or Lorentzian source distribution (see Section 4.1). The geometrical correction factor for N for a Gaussian source distribution [Goodman, 2000:242] is

$$N_{eff} = \left\{ erf\left(\sqrt{\pi}N\right) - \frac{1}{\pi}N^{-2}\left[1-\exp\left(-\pi N^2\right)\right]\right\}^{-1} \tag{19}$$

For a Lorentzian distribution, it is

$$N_{eff} = \left\{ \frac{1}{N} + \frac{1}{2}\frac{1}{N^2}\left[\exp(-2N)-1\right]\right\}^{-1} \tag{20}$$

These correction factors allow perfect accuracy of speckle contrast computation from a simple count of the number of coherence areas if the boundaries are sharp and well-

defined [Goodman, 2000:242]. For the case of diffraction-dominated pixel viewing area, the final result is not exact, as the viewing area boundaries are not sharp, but it is still quite accurate as will be shown in the Results chapter. For now, suffice it to note that for a typical active illumination engagement, the reduction due to short coherence length and sloped target surface tends to dominate, as shown in Figure 2.2. Here, the speckle contrast drops below 0.5 due to surface slope alone by 5° degrees of slope with 1 mm coherence length, a 30 cm aperture, 1 μm wavelength, and 3 km range to target.

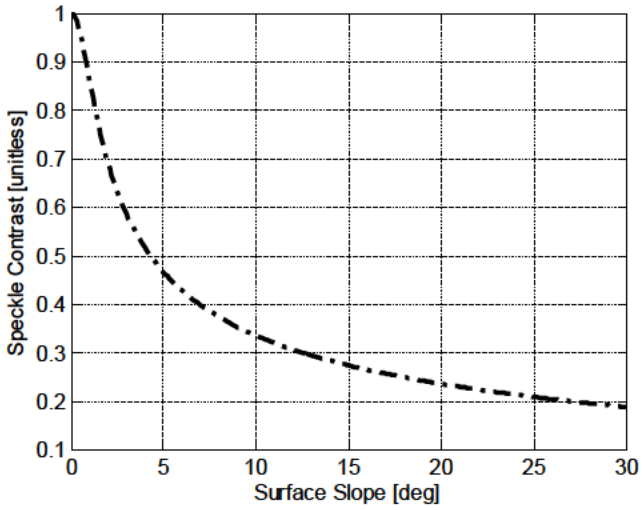

Figure 2.2. Speckle contrast reduction due to surface slope from the modified Huntley equation. Note that this reduction effect is considerably more significant than those considered previously. Conditions: Gaussian source spectrum, 30 cm aperture, 3 km range to target, 1 μm wavelength, and 1 mm coherence length.

Thus, active illumination speckle contrast reduction is caused primarily by three factors. The first two, polarization diversity and surface roughness, usually result in relatively small speckle contrast reduction of less than a factor of two. On the other hand,

the final factor, target surface slope, tends to result in a large reduction in speckle contrast under the likely condition that the target's surface normal differs from the look angle by more than a few degrees.

2.3 Combining Speckle Reduction Effects

Thus, under many conditions, speckle reduction due to surface slope is dominant. Even so, it is important to account for all speckle reduction effects simultaneously. This goal is accomplished through the straightforward multiplication of the numbers of degrees of freedom, N , due to the independent reduction effects of polarization diversity and combined slope and roughness, while the dependent effects of surface slope and roughness are combined in an RSS fashion according to

$$N_{total} = N_P \left(1 + \sqrt{\left(N_{eff} - 1 \right)^2 + \left(N_R - 1 \right)^2} \right) \tag{21}$$

where N_{total} is the final value for N which accounts for all effects, N_P is the value due to polarization diversity, N_{eff} is the corrected value due to surface slope, and N_R is the value due to surface roughness [Goodman, 2007:186]. Both the computation of N_P and N_R and the final computation of speckle contrast are accomplished using the common approximation for speckle contrast given N , $C \approx 1/\sqrt{N}$ (Eq. (17)).

2.4 Speckle Irradiance PDF

While speckle contrast provides information regarding the lower order statistics of speckle irradiance, the statistics are completely defined by the probability density function (PDF). While the PDF for a speckle field experiencing contrast reduction due to

the combination of a sloped surface target and a short coherence length source is not available in the literature, under the simplifying approximations of the modified Huntley equation, the equation for speckle irradiance PDF is well-known. Under these approximations, the irradiance PDF, $p_I(I)$, is found to be gamma distributed

$$p_I(I) = \left(\frac{N}{\langle I \rangle}\right)^N \frac{I^{N-1}}{\Gamma(N)} \exp\left(-N\frac{I}{\langle I \rangle}\right) \tag{22}$$

where N can be either N_{eff} if only surface slope contributes to speckle reduction or N_{total} if multiple factors come into play, and $\langle I \rangle$ is the mean irradiance [Goodman, 2000:247; Goodman, 2007:42].

2.5 Speckle Size

Another property of speckle which is of prime interest to active tracking work is the size of the speckles in the image. Because all detectors and most tracking algorithms involve some degree of spatial integration, they inherently reduce the impact of speckle. However, to determine whether or not that reduction might be significant, it is necessary to know the size of the speckles.

The classical van Cittert-Zernike theorem can be applied to this end. It gives an expression for mutual intensity (aka amplitude autocorrelation) given the intensity distribution of an incoherent source. However, this theorem makes several assumptions which must be evaluated for tactical tracking engagements. First, the theorem assumes that the wavefront leaving the target contains the effects of many scattering features. This condition is clearly satisfied for almost all active tracking engagements due to the long ranges and small (usually microscopic) sizes of surface features. Second, the illumination

and aperture areas must be much smaller than the range to target ensuring that only small angles are present. Once again, this condition is easily satisfied for active tracking. Finally, the illumination area must be very broad compared to the pixel field of view on target. Again, this condition is easily satisfied, as HEL systems typically use much smaller apertures for illumination than for imaging, but still warrants some further discussion [St. Pierre, 1997; Post, 2004]. It essentially ensures that a large number of speckles are present across the imaging aperture, which in turn implies a large number of coherence areas across the aperture. Under such conditions, the aperture itself can be treated as a spatially incoherent source, and van Cittert-Zernike can be applied to the propagation from aperture to image plane. Thus, the requirements of this theorem are satisfied for the vast majority of active tracking scenarios.

Having justified the use of the van Cittert-Zernike theorem, it can now be applied to evaluate speckle size and irradiance autocorrelation in the image plane. The theorem states that the field amplitude autocorrelation function is simply a scaled Fourier transform of the irradiance distribution, in this case, the irradiance distribution just past the imaging aperture. Using this result, assuming a circular aperture, and removing the mean irradiance, the speckle irradiance normalized covariance function $c_I(r)$ is given by

$$c_I(r) = \left| 2\frac{J_1\left(\frac{\pi D r}{\lambda z}\right)}{\frac{\pi D r}{\lambda z}} \right|^2 \tag{23}$$

where J_1 is a Bessel function of the first kind, order one, and r is radial distance [Goodman, 2007:77]. Note that this function is circularly symmetric. Also, normalized covariance is little different from autocorrelation $\Gamma_I(r)$ and is related to it according to

$$c_I(r) = \frac{\Gamma_I(r) - \langle I \rangle^2}{\langle I \rangle^2} \tag{24}$$

Speckle size follows from this result. First, recognize that normalized covariance is equal to complex correlation coefficient magnitude squared. Thus, Goodman's definition of coherence area applies [Goodman, 2000:210]:

$$A_c \equiv \iint \left|\mu(\Delta x, \Delta y)\right|^2 d\Delta x d\Delta y = \iint c_I(\Delta x, \Delta y)\, d\Delta x d\Delta y \tag{25}$$

The resulting coherence area is

$$A_c = (\lambda z)^2 \Big/ \left(\pi/4 D^2\right) \tag{26}$$

From the equation for irradiance covariance, the speckles will clearly have circular symmetry. Thus, speckle radius, r_s, is given by

$$r_s = \frac{2\lambda z}{\pi D} \tag{27}$$

which can be thought of as approximately a $1/e$ radius of speckle irradiance autocorrelation.

III. Experiment Methodology

A laboratory experiment was conducted for the purpose of partial model validation. In particular, validation of the dominant contrast reduction effect for active illumination, surface slope, was desired. As a further benefit, this experiment will fill in a gap in published work, as validation for the imaging geometry has not yet been published, and limited similar experiments have been published to date [Parry, 1975:88-115; Tchvialeva, 2008].

A 670.96 +/- 0.10 nm wavelength diode laser with short coherence length was used to illuminate a rotating rough surface, as is shown in Figure 3.1. The diode was a Toshiba T0LD9200 laser mounted to a thermoelectric cooler (TEC). Both diode current and temperature required precise control to maintain stable output power and coherence over the length of time needed to measure speckle for a particular slope angle. For this experiment, the current and temperature were set to 56.0 mA and 17.00°C respectively, producing a coherence length of 259 +/- 7 μm. After the beam left the laser, it was clipped by a 3.08 +/- 0.05 mm aperture to remove some of the side lobes of the multiple-transverse-mode beam. This truncation had no effect on irradiance in the central lobe on target, but only served to reduce stray light. It also did not alter the roughly elliptical laser beam shape. The beam then encountered an anamorphic prism pair, which shrunk the long dimension of the elliptical beam and produced a more circular beam of about 1 mm diameter. This small beam then propagated 3.778 +/- 0.016 m to a negative lens. The long propagation guaranteed spatial coherence, as will be discussed later and as is typical of HEL active illuminators, which use larger apertures for imaging than for illumination.

The negative lens further expanded the beam before it struck the rough surface to ensure adequate irradiance uniformity, as will also be discussed later. A silver-coated diffuse reflector (220 grit) was chosen as the target for its high reflectance in the visible and fairly Lambertian bidirectional reflectance distribution function (BRDF). It was rotated about the surface normal between image captures to randomize the rough surface features seen by each pixel, thus randomizing the speckle field and obtaining more independent speckle samples. The process of recording the speckle patterns for many rotation angles was repeated for surface slope angles of 0° to 15° to vary the observed speckle contrast.

Light scattered off of the target was reflected towards the detector by a mirror. Prior to reaching the detector, any depolarization due to the rough surface was removed by a linear polarizer. This process greatly simplified the data analysis. The light propagated 2.934 +/- 0.018 m before passing through an aperture of 2.72 + 0.03 mm diameter and positive lens of 20 cm focal length. The detector (a Marlin F131B connected to Matlab® via Carnegie Mellon University's FireWire Camera Driver) lay in the image plane of this lens to record the speckle irradiance. This detector had the cover glass removed to eliminate any interference effects other than speckle which tend to occur with coherent imaging using a standard complimentary metal-oxide semiconductor (CMOS) camera.

The experimental design involved the careful balancing of many competing factors, some of which were just mentioned in the description of the layout. The factors balanced are discussed in the following sections and were the number of speckle samples obtained, laser power and coherence length, spot size, target reflectance, speckle size, and pixels per speckle width.

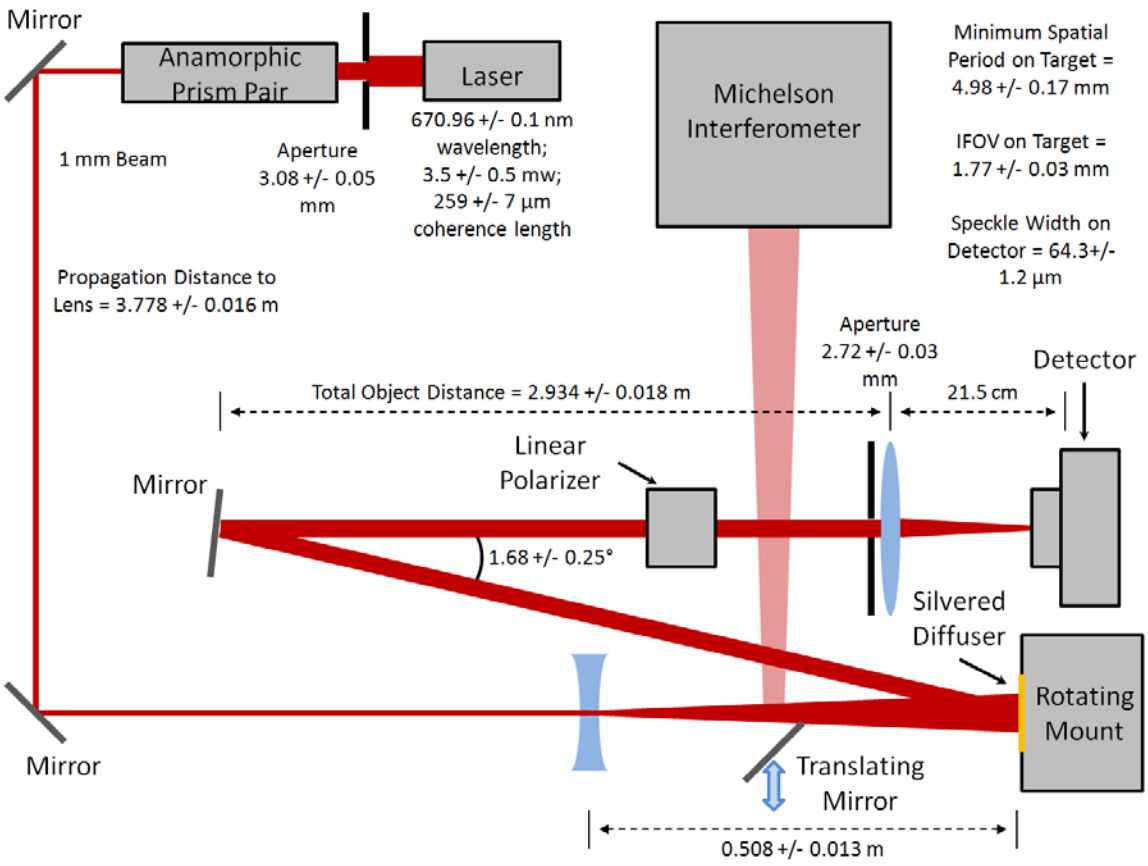

Figure 3.1. The experiment layout for speckle image model validation. The diverging laser beam either propagated to the silvered rough surface for speckle measurements or was deflected by a translating mirror to a Michelson interferometer for coherence length measurement.

3.1 Required Number of Speckle Samples

First, the number of speckles present in each recorded image was chosen to be 20. For statistical purposes, a large number of samples is desirable to reduce the error bounds on the computed mean and variance. However, obtaining more speckles per image requires a wider illumination area on target, thus spreading the laser power over a wider area and reducing the number of photons reaching each pixel of the detector. The number

20 was chosen such that sufficient photons reach the pixels to provide a mean SNR much greater than 1. After experimentation began, this number was increased to about 150 to satisfy irradiance uniformity requirements to be discussed later, considerably reducing mean irradiance. Figure 3.2 shows a typical speckle image with about 150 speckles within it. The masking which is clearly visible in this figure was done at the half irradiance point, as determined from the mean irradiance estimate to be discussed shortly.

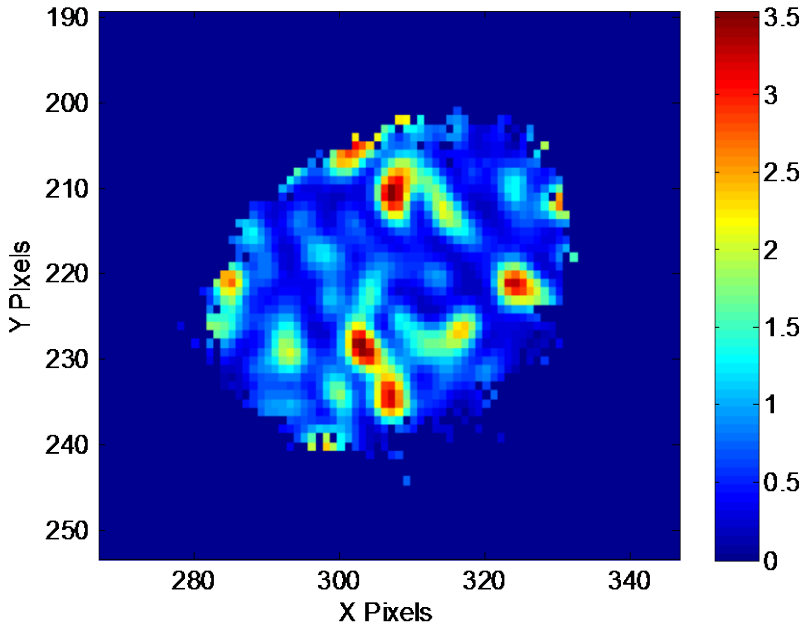

Figure 3.2. A typical speckle measurement. Here, the surface slope is 6° ($C \approx 0.73$), and the threshold for masking based on mean irradiance is set to 0.5 times the peak mean irradiance. Irradiance is normalized by the mean pixel irradiance. Approximately 150 independent speckles are present. Keep in mind that a speckle can be bright, dark, or intermediate.

The number of speckle samples required is driven by the need to reduce the error bounds, not about the computed mean or variance, but about the computed speckle

contrast. Because the speckle contrast of the intensity sum of *N* independent speckle fields is gamma distributed, the standard error equation developed for Gaussian distributions does not apply for the small values of *N* encountered during these experiments, though by the central limit theorem, it does apply for large *N*. The accepted convention is to use numerical analysis to estimate the error bounds [Tchvialeva, 2011]. In this work, the error bounds were estimated numerically using a Matlab® script (numberOfSamplesRequired.m in Appendix B). The script first creates a large number of random speckle irradiances for *N* coherence areas. This step is accomplished by propagating *N* randomly rough phase screens through an aperture sized to produce 4.8 samples per speckle, which matches the experiment conditions, and averaging the results. This process is repeated many times to generate the required number of speckle samples. The samples are divided into groups of *M* speckle samples, and the *M* values are used to compute speckle contrast of each group. By doing this for 1,000 groups of *M* speckle measurements, the standard deviation of the groups' contrasts about the mean speckle contrast is computed with little error. The error bounds are then defined as +/- one standard deviation about the mean. They are greatest for $N = 1$, or fully developed speckle [Tchvialeva, 2011], where 1,790 speckle samples results in error bounds of +/- 1.9% (2-sigma). The error bounds were seen to drop with increasing *N*, falling to +/- 0.8% by $N = 4$.

Since each image produced only about 150 speckle samples, 12 independent images were taken for each slope angle. Given a 25.4 mm diameter target utilized to 12.7 mm diameter and about a 1.74 mm diameter pixel viewing area on target, up to about 23 unique speckle patterns can be obtained simply by rotating the target surface between

image captures. During the actual experiment process, 12 measurements were taken, producing about 1,800 independent speckle measurements and reducing error bounds sufficiently.

It should also be noted that source irradiance was quite non-uniform across the target area. The target rotation also allows for removal of this non-uniformity. By rotating the target smoothly about its normal while taking 400 speckle images, then averaging the speckle images together, estimated pixel values proportional to the mean irradiance on target were found. A typical mean irradiance estimate is shown in Figure 3.3. Note that some pixel-by-pixel or "salt and pepper" noise is still visible even after averaging 400 images, possibly due to detector non-uniformity rather than read-out noise. Regardless, detector non-uniformity is removed by normalizing to mean irradiance computed in this way. Further, the effects of slowly varying dark current noise (horizontal banding) are visible around the $1/e^2$ irradiance levels due to the long integration times and high gain levels needed to compensate for very low irradiance on target.

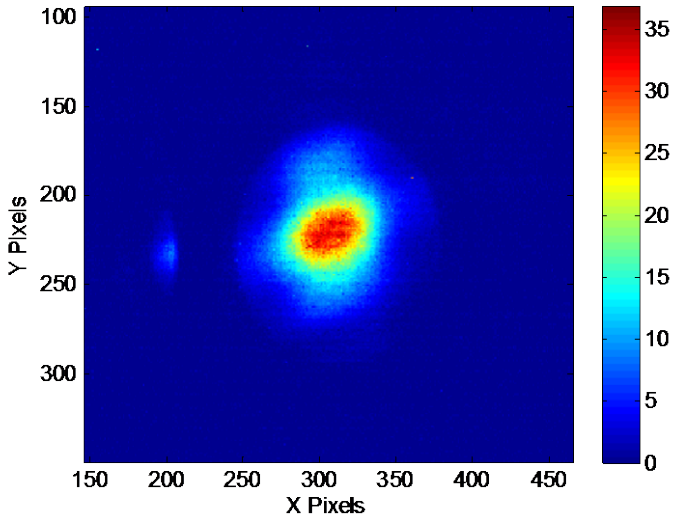

Figure 3.3. An estimate of mean irradiance on target given in digital counts. The surface slope is 6°, and 400 images were taken as the surface was rotated and averaged to estimate the mean.

3.2 Speckle Spatial Sampling

The speckles also needed to be resolved on the FPA in order to obtain good contrast measurements. One way to think about this fact is to consider that if many speckles form across each pixel, then they are averaged together, and the number of independent speckles contributing to each pixel is greatly increased, skewing the statistics. Measuring the core speckle statistics requires much less than one speckle per pixel. Another Matlab® script was used to address this issue (speckleSpatialSampling_testOfPixelAveraging.m in Appendix B). This script also defined a uniform amplitude source field with delta-correlated random phase and propagated it through an aperture to a focal plane. Different values of *N* were evaluated by averaging multiple independent speckle patterns together. It was found that two samples per speckle yields a deterministic contrast error of about -10.5%, four samples yields -2.6%, and eight samples yields -0.65% contrast error regardless of the value of *N*. Furthermore, error was found to decrease linearly with the square of the pixels per speckle. Because the error is a constant offset, it is easily removed from the experimental data. Even so, keeping the error small allowed more straightforward troubleshooting of the experimental layout. Thus, 4.80 pixels per speckle width were chosen, producing a constant error of -1.81%. This bias was removed from the final data set. Figure 3.4 shows an example speckle irradiance autocorrelation from a single speckle measurement set. The speckle width is observed to be about 4.8 pixels as expected.

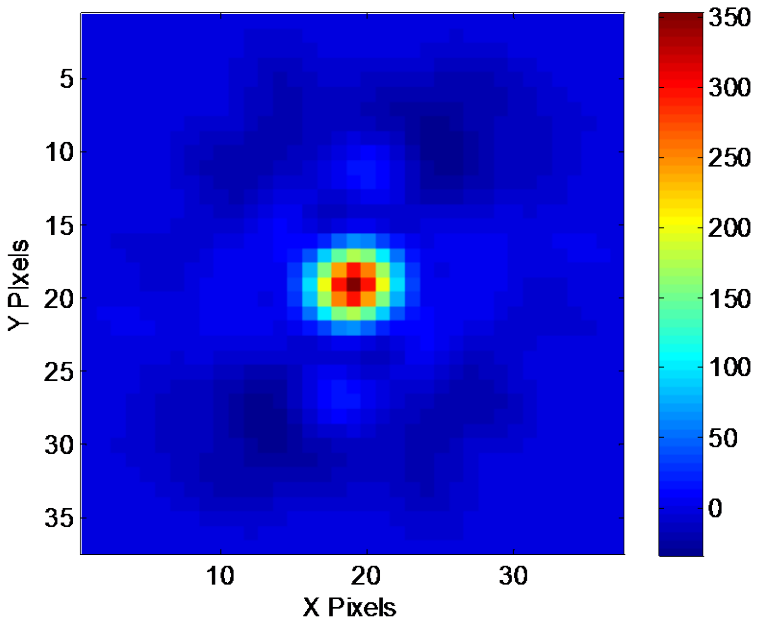

Figure 3.4. Speckle irradiance autocorrelation for a single speckle measurement set at 0° slope. The width of the autocorrelation is a measure of speckle width and is about 5 pixels (taking λ/D as speckle width).

3.3 The Imaging Setup

In order to properly resolve the required number of speckles while maintaining enough energy per pixel for imaging, the imaging setup had to be very carefully selected. See the Matlab® script imagingScenario.m in Appendix B for a numerical investigation. Assuming a detector with 13.4 µm pixel pitch, a source with wavelength of 670.96 nm, an aperture with diameter 2.72 mm, and source projecting 1.5 mW onto the full width half maximum (FWHM) beam area on target, then the aperture-to-FPA distance had to be about 0.20 m and the object distance 2.934 +/- 0.018 m. To be more precise, the 1:14.7 ratio was critical, while the exact distances could be scaled up or down to match the physical constraints of the lab and hardware. The speckles were 64.3 +/- 1.2 µm wide in size on the FPA, and the pixel size on target (IFOV) was 1.77 +/- 0.03 mm. If the source

intensity is spread over about 1600 pixels for a 9.6 cm beam diameter on target, giving 150 speckle samples, then the irradiance at each pixel should be about 1.15 nW/mm^2. While the minimum detectable irradiance for the Marlin detector used in this work was not known, a similar CMOS device had SNR = 2 at 2 nW/mm^2 (DCC1545M) [Thorlabs, 2014]. Thus, the speckle irradiance is barely detectable above the noise. In practice, each speckle measurement was taken 20 times and averaged together to reduce the noise by about a factor of 4.5. Additionally, operation at slope angles at or below 15° for the rough surface, which is not perfectly Lambertian, provided some additional irradiance beyond that predicted by the Lambertian assumption used here.

3.4 Coherence Area on Target

In tactical active tracking for an HEL weapon, one would expect that the coherence area of the illumination on target would be greater than the IFOV, as the illuminator aperture is usually considerably smaller than the imaging aperture [St. Pierre, 1997; Post, 2004]. In order to guarantee that this condition was also satisfied in the experiment, the illumination beam was propagated far enough to ensure a coherence area greater than the pixel viewing area. A worst-case spatially incoherent source, such as an LED, was assumed. Then, the van Cittert-Zernike theorem was used in conjunction with the definition of coherence area, $A_c \equiv \iint \left|\mu(\Delta x, \Delta y)\right|^2 d\Delta x d\Delta y$, where $\mu(\Delta x, \Delta y)$ is the complex coherence factor, to define the coherence area of a uniformly bright source of any shape and with area A_s as

$$A_c = \frac{(\lambda z)^2}{A_s} \tag{28}$$

Given a propagation distance, *z*, of 3.778 m and source area of 8.28e-7 m^2, the coherence diameter assuming circular symmetry was 3.1 mm at the negative lens (see Figure 3.1), which was then expanded by the lens to 6.3 mm, much larger than the pixel viewing width of 1.77 mm. Thus, a source propagation distance of 3.778 m ensured good spatial coherence across each pixel's viewing area.

3.5 Irradiance on Target

Finding a source to satisfy the previously defined requirements proved challenging. It was established that about 1.5 mW of irradiance needed to fall over an area of 9.6 mm diameter on target to get enough photons to the detector. However, coherence length also needed to be kept short, on the order of 100 – 300 μm, to get multiple coherence areas within the IFOV due to surface slopes in the range 0° to 15°. Two source options were considered. First, LEDs have coherence lengths on the order of 10 μm, which is so short that the slope of the target would need to be measured very precisely to keep error bounds small. Alternatively, LED coherence length can be increased to > 100 μm with use of a narrow band spectral filter which attenuates away most of the light. The LED would need > 50 mW of power for such use. Very few LED options exist which meet these requirements (50 mW power with peak emission near 632.8 nm to allow use of a 1 nm laser line filter, and < 30° divergence to allow collimation) including the Vishay VLCS5830 and Avago HSMC-A431-X90M1 which would have to be tested to determine whether they meet the requirements in practice, and even if they do, do not provide a power advantage over the laser sources discussed later. Another strike against an LED source is the fact that they are incoherent sources with

fairly large emission area and high divergence, making collimation difficult. If collimated using an f = 11 mm aspheric lens to 1.5 mm diameter (for a very narrow 8° divergence LED), over a propagation of 2 m (required for spatial coherence) and assuming a 500 μm die size, the LED irradiance would spread to 9.1 mm. Prior to starting the experiment, the planned beam size on target was much smaller than 9.1 mm, and only later was the experiment redesigned to allow such a beam size. Thus, while LEDs may be just adequate to meet the needs of this experiment, none were tested due to the difficulties regarding coherence length and collimation.

The other option considered, and the one chosen, was the diode laser. Inexpensive diode lasers often have coherence lengths between 100 μm and 3 mm [Rotge et al., 1992; Deninger and Renner, 2010]. Further, diode coherence length can be decreased by reducing diode current below the nominal value [Rotge et al., 1992]. Additionally, diode lasers can be well-collimated through use of an aspheric lens, as they have relatively small emission areas. Thus, a diode laser can provide both high power on target and low coherence length with considerably fewer complications than encountered with an LED.

As was mentioned, it was not initially apparent that the beam needed to be expanded to 9.6 mm FWHM on target. It was initially theorized that a beam diameter of half that value would be sufficient to ensure adequate irradiance uniformity over each pixel's viewing area of 1.74 mm. However, after dozens of failed attempts to obtain speckle contrast near unity for 0° slope, it was observed that the main lobe had fine irradiance variations at higher spatial frequencies than could be resolved by the imaging setup. This fact may have been due to the multiple-transverse-mode diode laser. Regardless, greatly expanding the beam beyond the initial plan allowed speckle contrast

to rise significantly closer to unity. For the final layout, the laser beam was first propagated 3.778 m to allow diffraction to blur out the high spatial frequencies before expansion by about a factor of 2 using a negative lens. The negative lens further expanded the beam beyond the limits of diffraction, as propagation over more than 4 m was not feasible due to laboratory space limitations. With this configuration, speckle contrast near unity for 0° slope was obtained.

3.6 Coherence Length Measurement

Prior to starting experimental work, it was not known what type of laser would provide the necessary coherence length, though diode lasers were considered a prime candidate. Thus, many lasers had to be tested. Ultimately, the Toshiba T0LD9200 671 nm diode laser proved to be an acceptable source. The coherence length of a diode laser can vary over time due to thermal changes. For this reason, prior to taking any measurements, the diode was turned on and allowed to cool down (TEC cooled) to steady state over a period of at least 10 minutes. The coherence length was then measured for each start-up of the diode using a Michelson interferometer. The source beam was diverted to the interferometer by adding a mirror. Coherence time was computed from the complex degree of coherence according to

$$\tau_c \equiv \int \left|\gamma(\tau)\right|^2 d\tau \tag{29}$$

where τ is the temporal difference. The complex degree of coherence was itself computed from the fringe visibility according to

$$\gamma\left(\frac{2h}{c}\right) = V(h) \tag{30}$$

where h is the path difference. V is the fringe visibility, defined by

$$V \equiv \frac{I_{\max} - I_{\min}}{I_{\max} + I_{\min}} \tag{31}$$

where $I_{\max}$ and $I_{\min}$ are the maximum and minimum irradiance in the fringe pattern respectively [Goodman, 2000:158-168].

The first stage of the experiment involved testing the coherence length of various lasers using the Michelson interferometer. Lasers tested included five laser pointers, one laser module, and one diode laser. The laser pointer wavelengths tested included samples in the blue, green, yellow, and red spectral bands, and all exhibited similar coherence properties with fringe contrast dropping from a peak to a minimum over about 1.3 mm of optical path length difference before rising again. This periodicity is caused by the multiple longitudinal modes characteristic of diode lasers. The modes are widely spaced due to the short effective cavity length of diode lasers, creating a pseudo-discrete spectrum and producing coherence which drops off and rises again many times as path difference increases. The depths of the troughs and the heights of peaks varied from one unit to the next, but all exhibited troughs no less than 0.2 and coherence lengths in excess of 1 cm. Figure 3.5 shows fringe visibility versus optical path length difference for an Infiniter red laser pointer. The periodic fluctuations are clearly visible, as is the fact that coherence does not drop off much out to 1 cm path difference. Thus, coherence length of this unit was much greater than 1 cm, a characteristic common among laser pointers.

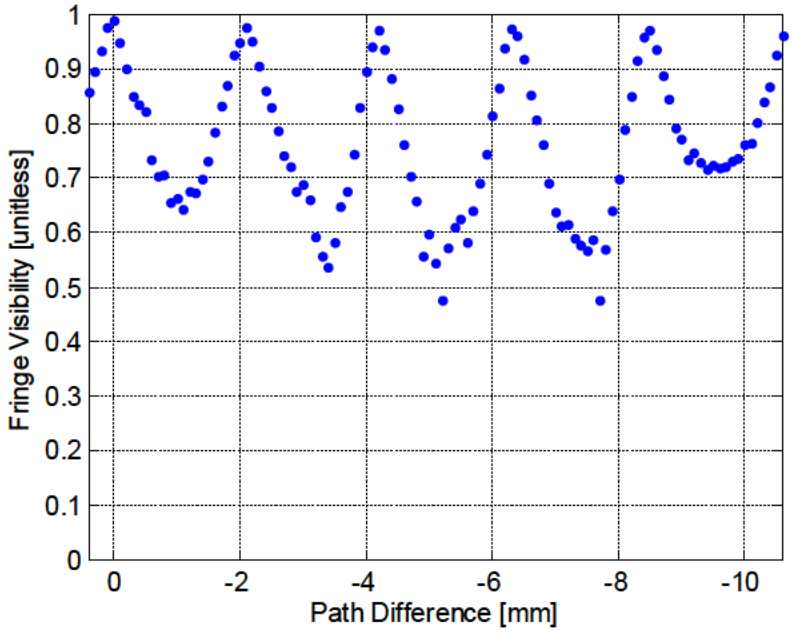

Figure 3.5. Infiniter red laser pointer fringe visibility. Note that coherence rarely drops much below 0.6 over 1 cm of path length difference, indicating that coherence length is much greater than 1 cm. However, a periodic fluctuation is also very apparent.

The next lasers tested were the diode laser module and the laser diode. The module proved to be very similar to laser pointers when operated at the rated voltage of 5.0 V. However, when operated at 3.3 V, the coherence length dropped down to the point that the diode may have been functioning as an LED rather than as a laser (coherence length of 10 to 20 µm). The module used a simple resistor to control current, and thus output power was greatly reduced at 3.3 V versus 5.0 V. Up to this point in the process, no acceptable lasers had been found, as a coherence length of 100 to 500 µm was needed with decent output power. However, the Toshiba T0LD9200 laser diode proved to be the answer. One of the first observations made with this diode was that the coherence length varied proportionally with output power. Thus, by controlling the drive current (and

output power), the coherence length could be adjusted to the desired value. The temperature also needed to be controlled to prevent mode hopping and increase the stability of both coherence length and output power. Drive current of 53.5 mA at 17.06°C produced coherence length of 125 +/- 7.8 μm and power of about 1.1 mW. However, more power was needed. At 56.0 mA and 17.00°C, the power was about 3.5 mW, while the coherence length was measured at 246 +/- 7 μm. The stability of the coherence length, assuming control of the drive current and temperature, was found to be very good with standard deviation of only 3.14% from measurement to measurement at 53.5 mA and 1.4% at 56.0 mA. Most of that deviation is probably due to measurement error, but separation of measurement error from coherence length drift was not achieved. Even so, such stability was more than adequate for this work. The one possible issue that remained with the T0LD9200 diode was that achieving short coherence required a reduction in output power from maximum. As was already noted, the 3.5 mW output proved to be just adequate to take measurements at low slope angles. Typical fringe visibility plots for the conditions previously described are shown in Figures 3.6 and 3.7.

The means by which coherence length was computed deserves some additional discussion. Obtaining good fringe visibility with the Michelson required a three step process. First, the cover was placed on the camera and thirty images were taken in rapid succession. These thirty images were then averaged together to form the dark image to be subtracted from all future images to increase accuracy. Second, the mean detected irradiance was found in a similar manner, this time by rapidly changing the path length difference, which moved the fringes across the detection area. Once again, many images were taken and averaged together, with the result being the estimated average irradiance.

This average irradiance was then used to normalize all measurements by the average irradiance detected by each pixel, effectively removing non-uniformity in both irradiance and detector response. Finally, the fringe visibility was computed for each path length difference by capturing seven images, averaging them to reduce shot noise, masking off only the region with mean irradiance above the $1/e^2$ irradiance level, and finding the minimum and maximum normalized irradiance for use in the fringe visibility equation.

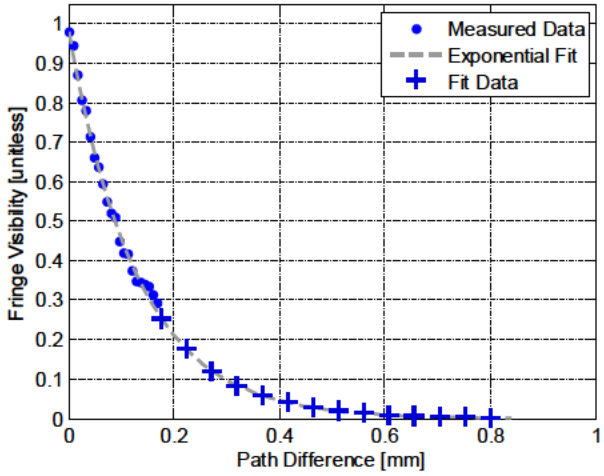

Figure 3.6. Toshiba T0LD9200 diode fringe visibility at 53.5 mA and 17.06°C as measured by a Michelson interferometer. Note the steady drop in visibility over a path difference much smaller than was considered for the diode pointer earlier. Coherence length is 125 μm at 1.1 mW output power.

As previously discussed, it is well known that fringe visibility has a direct relationship to the complex degree of coherence, which in turn is directly relatable to coherence length. However, the tails of the visibility were unmeasureable with the Michelson, as noise prevented accurate measurement of visibility below about 0.3. Still, the fringe visibility of this diode was found to closely follow an exponential decay above

that threshold. Thus, a curve fit was done, fitting an exponential to the measured data above 0.3 visibility. The curve fit provided the visibility values below 0.3. In general, using the curve fit data for the tails increased the total coherence length by about 8%.

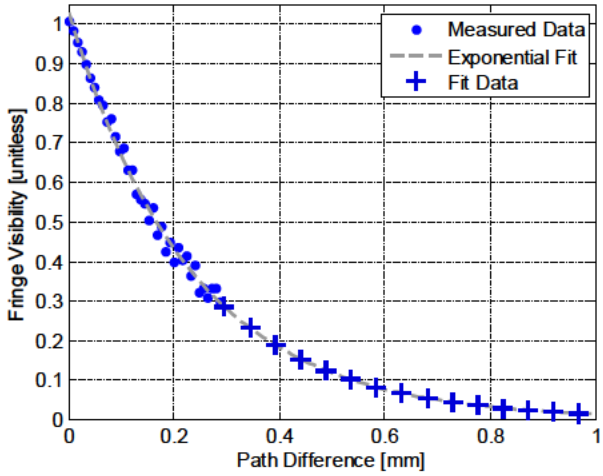

Figure 3.7. Toshiba T0LD9200 diode fringe visibility at 56.0 mA and 17.00°C as measured by a Michelson interferometer. Coherence length was measured at 246 µm, roughly double that of Figure 3.6 due to the increase in power to 3.5 mW.

Thus, using a Michelson interferometer with this procedure, the T0LD9200 was found to be adequate for this experimental work. Its coherence length was 246 +/- 7 µm at 56.0 mA drive current and 17.00°C according to the Michelson.

The power spectral density of the source was also measured using a Czerny-Turner spectrometer to validate the Michelson interferogram measurements. At first, a small unit (Thorlabs CCS175) was used, but its spectral resolution of ~0.5 nm FWHM was insufficient to properly measure the overall spectrum of the laser of about 0.6 nm FWHM, let alone to resolve the individual longitudinal modes. Thus, a 1.33 m focal

length McPherson 209 Czerny-Turner monochronometer was also used, and its results were found to be of adequate resolution of about 0.02 nm FWHM. A McPherson "snap-in" grating with 500 nm blaze, 1200 grooves/mm, and 110 x 130 mm size was used. Slit width was set to about 33.4 μm, thus filling the grating with light along one dimension. The monochronometer output was passed into a photomultiplier tube (PMT), chosen for its high dynamic range and SNR, which was in turn connected to a Keithley 486 Picoammeter.

The measurements of the diode laser's spectrum are shown in Figures 3.8 and 3.9. Figure 3.8 shows several notable features. First, the hundreds of longitudinal modes are indistinguishable in this figure due to their close spacing (about 0.17 nm). Second, the laser's spectrum covers a wide spectral range of several tens of nanometers, mostly due to the low power wings of the distribution. Finally, the laser spectrum rides upon a considerable plateau likely caused by some combination of the blurring together of the individual modes and some incoherent light output. Figure 3.9 shows the seven strongest modes in linear space. Here, the spacing of the modes is seen to be about 0.17 nm (or 110 GHz), while each mode has width about equal to that of the resolution of the instrument, indicating that the spectral profile of each mode is not well-resolved. The length of the optical cavity, L, can be calculated from mode spacing if the refractive index of the lasing material is known by using the well-known equation $L = c/2n\Delta v$, where n is the refractive index and Δv is the mode spacing in Hz. For this laser, the material is not known, but many common laser materials (such as gallium arsenide, indium phosphide, and gallium antimonide) have refractive index around 3.8, indicating that cavity length may be about 360 μm, which seems reasonable.

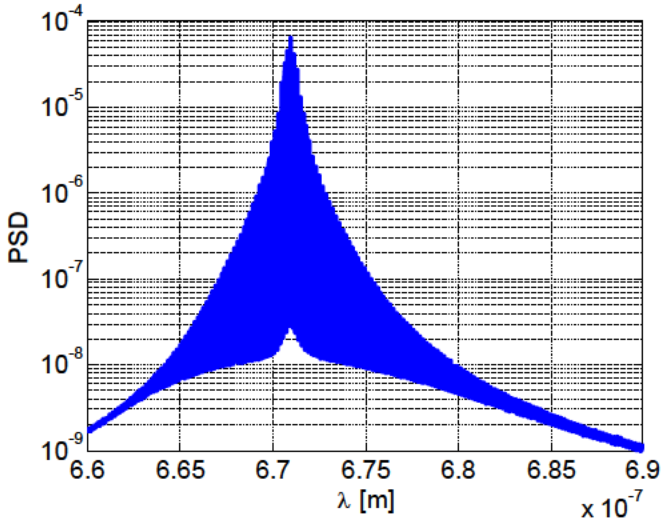

Figure 3.8. T0LD9200 diode laser spectrum in log space as measured by a McPherson 1.33 m focal length Czerny-Turner spectrometer. The hundreds of longitudinal modes are blurred together in this figure, but the overall profile in log space is apparent. The spectrum sits upon a strong pedestal caused by some combination of incoherent light output and the real blurring together of the closely spaced modes (about 0.17 nm apart). Further, the modes extend over quite a wide spectral range of several tens of nanometers.

It is worth mentioning that a spectral calibration of this data was performed using Krypton lines. A partial pressure Krypton pen light emitted into the instrument concurrently with the diode laser, and its well-known spectral lines were used to calibrate the output. Some of those spectral lines are shown in Figure 3.10. For the calibration, two Krypton spectral lines were used below 650 nm, and seven were also used above 700 nm. Because the Czerny-Turner spectrometer's output is very nearly linear in wavelength with grating rotation, a simple linear calibration was sufficient to reduce absolute wavelength error to a small fraction of a nanometer and relative wavelength error over the spectral range of the laser to much less than that. Further, because the PMT's

response was quite flat over the spectral region of interest, calibration of its irradiance response with wavelength was not necessary.

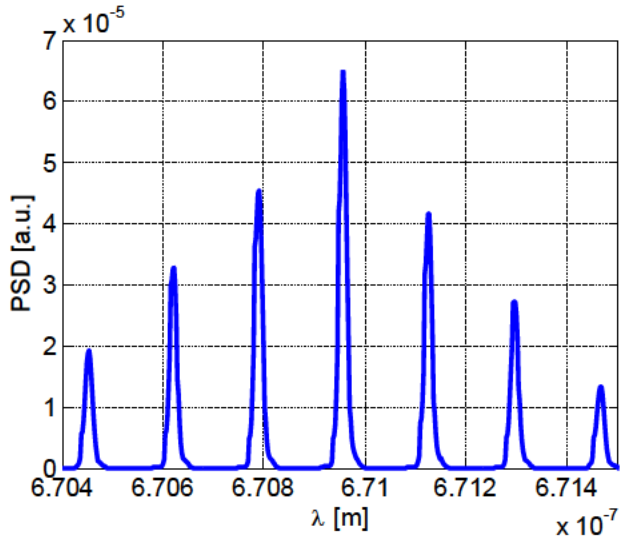

Figure 3.9. T0LD9200 diode laser spectrum in linear space showing only the seven strongest modes. The individual modes are separated by about 0.17 nm.

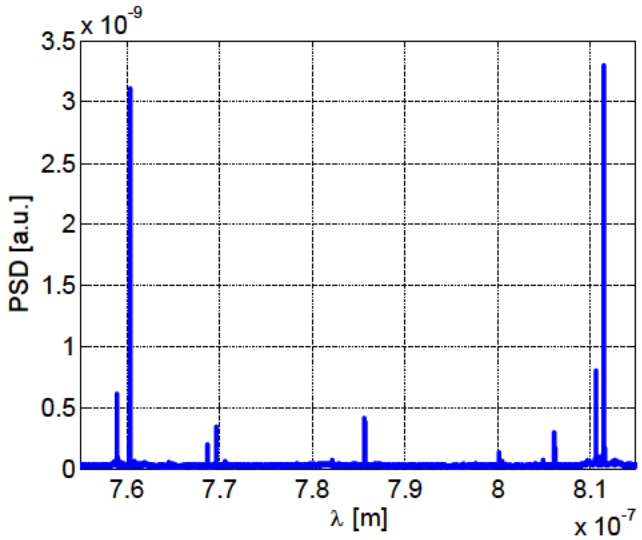

Figure 3.10. Spectral lines of the partial pressure Krypton lamp. These lines are readily apparent in the measurement of the diode laser spectrum. The highly linear response of the spectrometer in wavelength with rotation allowed a simple linear calibration based on such lines.

Further, the McPherson PSD measurements support the previous observation that coherence length increases with output power. Figure 3.11 shows a comparison of PSDs at four different power levels. The PSDs clearly become peakier as power increases. Stated differently, the maximum power density is increased, while the power in the wings remains about constant, indicating that coherence increases with power.

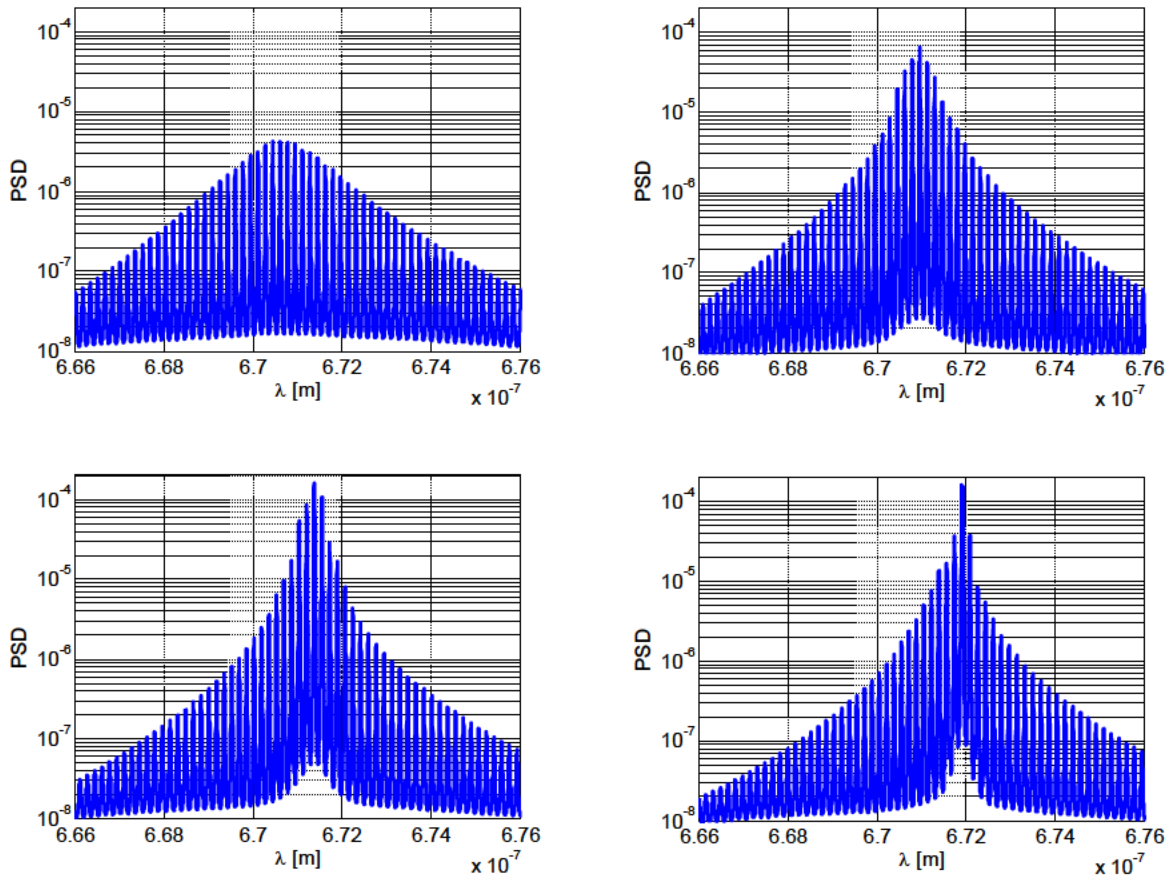

Figure 3.11. A comparison of diode laser PSDs at four different power levels. From left to right and top to bottom, the power levels are 1.1, 3.5, 5.9, and 9.0 mW respectively. Note that the spectrum narrows, with highs becoming higher, as power increases.

Fitting a Lorentzian to the measured PSD shows good agreement near the peak and some disagreement in the wings. Figure 3.12 shows such a fit. A moving average filter of width 100 (about 0.22 nm wide) was used to smooth the measured PSD. The Lorentzian fits the measured data very well near the peak of the distribution. However, out in the wings, the measured data is considerably lower than the Lorentzian model predicts. Further, the measured data shows asymmetry which is not captured by the Lorentzian, though this asymmetry may be due to the lack of PMT spectral response calibration, and it does not appear at all significant.

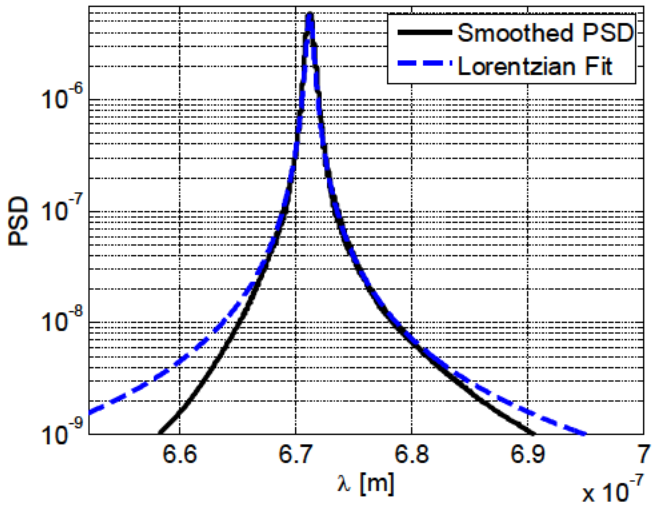

Figure 3.12. A comparison of the smoothed spectrometer PSD with a Lorentzian curve fit. The fit matches the data quite well near the peak, but the wings of the distribution show considerably lower power than modeled by the Lorentzian fit. Also, the wings show some asymmetry not captured by the Lorentzian. A moving average filter of width 100 (about 0.22 nm) was used here to smooth the measured PSD.

Of course, it is possible to compute the coherence length by converting the PSD to complex degree of coherence (which is normalized to have a peak value of 1; see

Figure 3.13) and integrating the absolute value squared over time difference. Such a procedure indicates a coherence length of 259 +/- 7 μm, which is 5.3% longer than measured with the Michelson interferometer. A comparison of PSD-based visibility and Michelson-measured visibility in Figure 3.13 reveals the cause of the difference. Primarily, the cause is the slightly higher visibility computed from the PSD than measured by the Michelson. Additionally, while an exponential decay curve fit was used to extrapolate the Michelson data beyond its noise limit of about 0.3, the PSD-based data shows a temporary leveling-off around 750 μm, which is of course not modeled with the exponential curve fit. These two causes of extra fringe visibility likely account for the slightly longer PSD-based coherence length and should represent reality. Of note, the PSD-based fringe visibility also needs to be cutoff at some point in the coherence length integral to avoid integration over more than one of the multiple coherence peaks which result from the discrete spectral nature of the lasing modes. Here, it was cutoff at 1 mm path difference, the largest difference likely to have any significant impact on speckle contrast results for surface slopes up to 15°. Still, even integrating out to 2 mm path difference only increased coherence length from 259 to 262 μm.

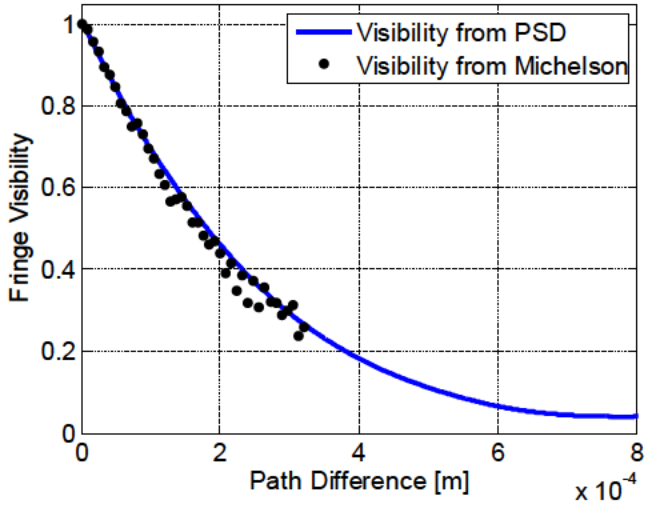

Figure 3.13. Fringe visibility based on the PSD measurement compared to Michelson interferometer measurements. The PSD-based visibility indicates a coherence length of 259 μm, while the Michelson-based result, after exponential decay extrapolation, indicates 246 +/- 7 μm. The difference is likely mostly caused by the slightly higher fringe visibility computed from the PSD than measured by the Michelson.

3.7 Temporal Stability of PSD

It was important that the spectral output of the diode laser either remains almost constant over time or changes rapidly enough that each speckle measurement effectively used the long time average PSD, such that there would not be differences in the PSD from one speckle measurement to the next. To investigate, a Thorlabs CCS-175 compact Czerny-Turner spectrometer was used to observe the PSD stability over time. While its resolution is poor compared to the McPherson instrument, its silicon detector array allowed variations on integration time which were not permitted with the PMT-based scanning McPherson. Six measurements were taken over a period of 34 minutes and with both 50 μs and 40.96 ms integration times. The former corresponds to the shortest integration times used during this work (for some of the Michelson interferometer

measurements), while the latter corresponds to the longest (for the speckle images). In all cases, the PSD variation was almost imperceptible from one measurement to the next. Maximum and minimum computed coherence lengths were less than 2% different. Figure 3.14 shows an example of such variation between measurements, and in this case the difference in computed coherence length is only 0.33%. Note that individual laser modes are not visible due to the instrument's wide resolution of 0.5 nm FWHM. The excellent stability is likely due to the TEC used to stabilize the diode temperature and prevent mode hopping.

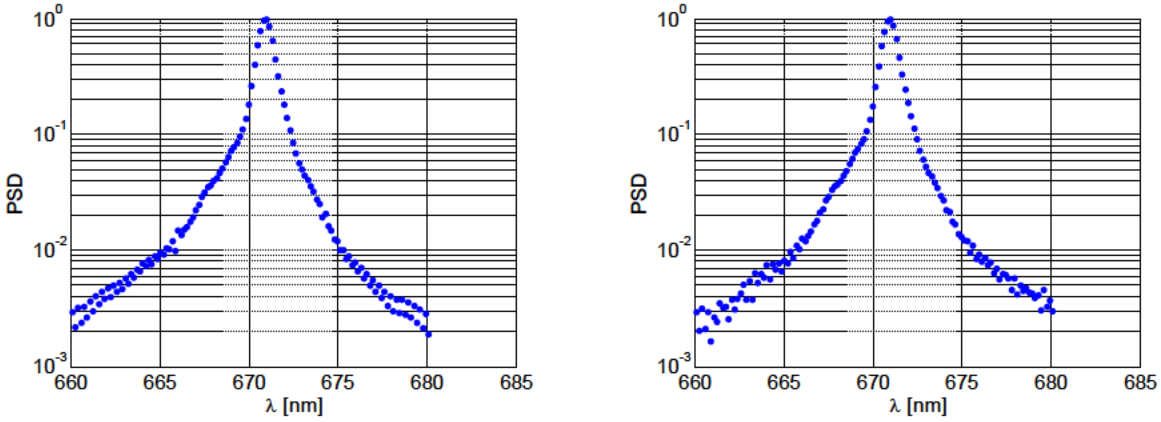

Figure 3.14. Two PSDs captured with different integration times. The left plot was taken with 50 µs integration time, while the right plot was taken with 40.96 ms integration time. The differences are insignificant. Computed coherence length changed by only 0.33% between the two measurements, indicating good temporal stability.

3.8 Target Surface Properties

The physical properties of the rough surface target (shown in Figures 3.15 to 3.17) are also of some importance. For one, the surface height standard deviation is an input to both Hu's theory for speckle contrast reduction and the theory regarding contrast

reduction due to surface roughness. Further, all of the speckle theory discussed here assumes that many rough surface features are visible to each pixel, implying that the surface correlation length is much less than the IFOV. Thus, the standard deviation and correlation length of the rough surface were measured using a profilometer.

A Zeiss microscope captured images of the rough surface target at varying magnifications, as shown in Figures 3.15 to 3.17. The target was illuminated from the front using a source with a yellow tint. Combined with the response of the camera used, this yellowish source produced images with an apparent gold tint. Perhaps the most important take-away from these figures is that the surface appears to be free of uncoated patches and significant defects in the coating.

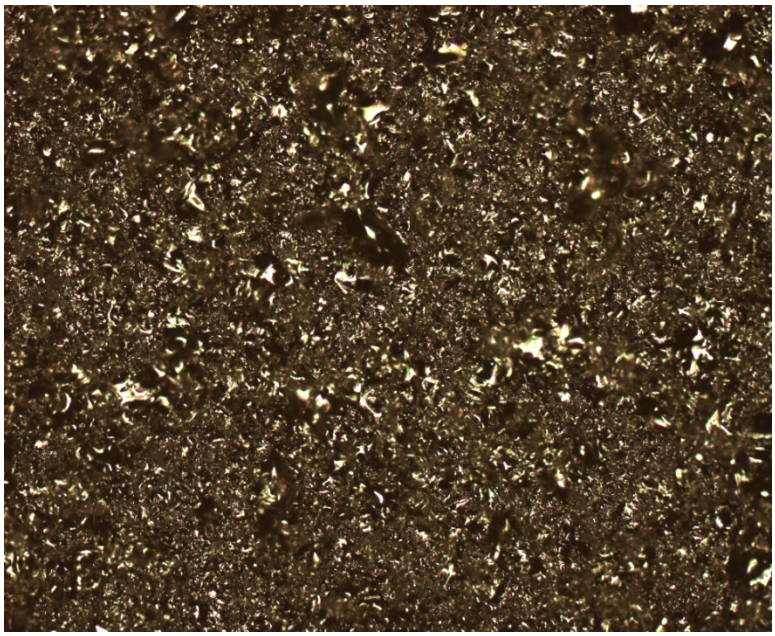

Figure 3.15. The silver-coated 220-grit diffuse target as viewed by a microscope. The apparent gold tint is due to a combination of illuminating light with a yellow tint and the camera. To the naked eye, the surface appeared quite silver. Magnification here is 10x.

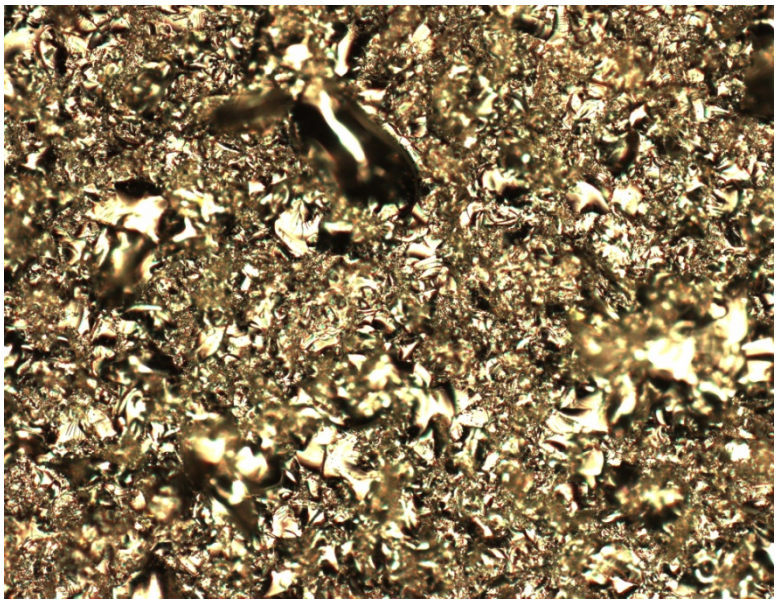

Figure 3.16. The rough target at 20x magnification. Note that the tallest surface features are now out of focus.

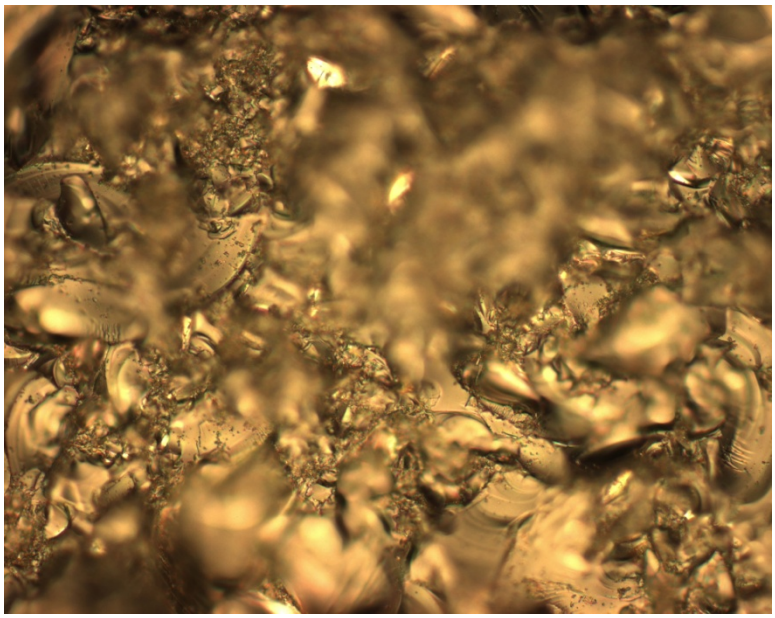

Figure 3.17. The rough target at 50x magnification. Note that the surface appears to be cleanly coated in silver. No major imperfections are visible.

The statistics of the rough surface were computed from the profilometer measurements. An example of the measured surface profile over a 10 mm span is shown in Figure 3.18. Because the profilometer surface was not level, no information regarding gross surface slope was obtained. Rather, all measured slope was removed from the data, which was taken near the center of the target. The peak to null correlation was measured at 122 μm, as shown in Figure 3.19. Surface height standard deviation was 3.27 μm.

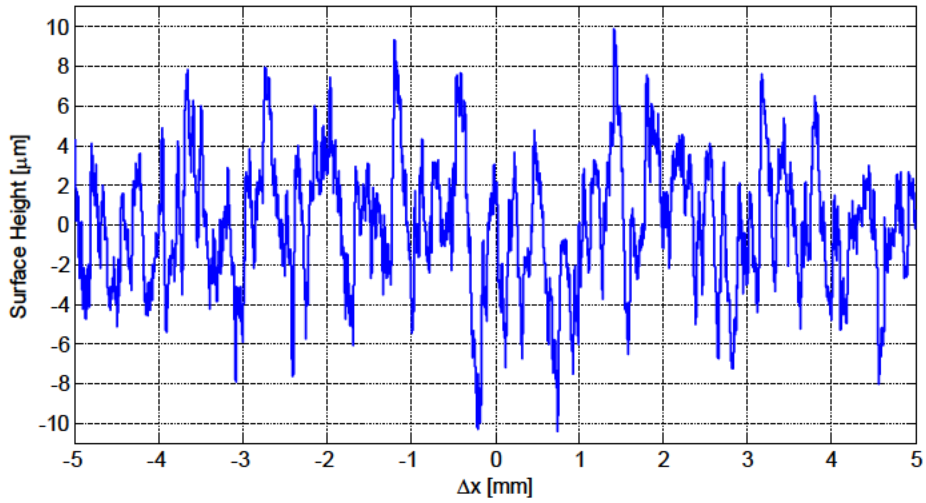

Figure 3.18. A profilometer measurement of surface height near the center of the 220 grit silvered diffuser target. The profilometer was not leveled prior to measurement, but rather all measured slope was removed from this data.

Regarding the number of rough surface features seen by each pixel, the surface autocorrelation is shown in Fig. 3.19. Measured autocorrelation one-sided width was 122 μm. Since each pixel saw about a 1.77 mm diameter region on target, approximately 200 independent rough surface features were visible to each pixel, which is sufficient to make the necessary large number approximations with little error.

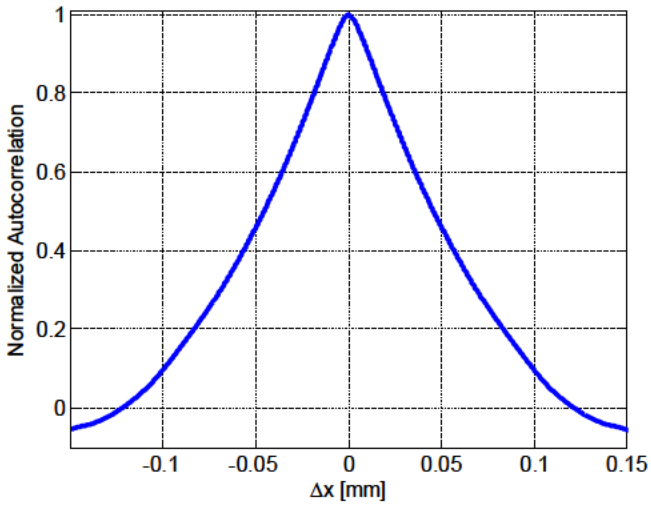

Figure 3.19. Surface height autocorrelation as a function of linear displacement. The peak to null width is 122 μm.

Further, the common approximation regarding surface height distribution is that it follows a Gaussian function. Figure 3.20 supports that assumption for this surface. While more data points would be necessary to determine exactly how close the surface height is to Gaussian, the available data clearly shows a Gaussian-like distribution. Thus, having investigated surface height distribution, standard deviation, and correlation length, all necessary properties of the surface are defined.

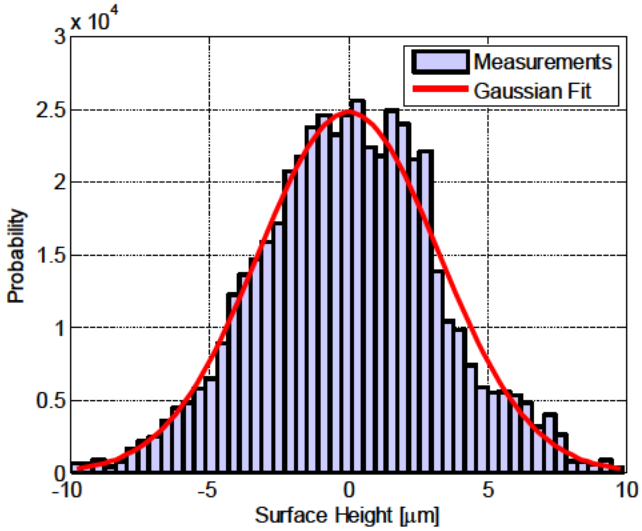

Figure 3.20. Rough surface height distribution with a least-squared error Gaussian curve fit overlay. The data does seem to fit a Gaussian distribution, though more samples would be necessary to verify that theory. The standard deviation of the measurements is 3.27 μm, while the mean is only 7 picometers.

3.9 Experiment Procedure

In the previous discussions regarding optical layout parameter selection, the topic of experimental procedure came up occasionally and is now discussed in more depth. To begin experimental measurements, the diode laser source and temperature controller were first turned on at least 10 minutes prior to taking any measurements so that it could reach optical and thermal steady state. Next, the laser coherence length was measured via a Michelson interferometer (see Section 3.6). After that, the path from the imaging lens to the detector was shielded from stray light using a combination of lens tubes and cardboard, and the room lights were turned off, making the laser light the vastly dominant source of target illumination.

Speckle measurements were then taken. First, a dark image was captured by blocking the laser light near the source, capturing thirty images, and averaging those

together to reduce shot noise. This dark image was subtracted from all subsequent speckle measurements to reduce the dark current noise (aka fixed pattern noise). Next, the target surface slope was adjusted to the desired angle, and the detector gain and integration time were set such that saturation was only just avoided, thus utilizing the full detection range and minimizing the impact of quantization of detected irradiance to an 8-bit number. Speckle was then measured by taking a series of 12 sets of images at different axial rotation angles from 0° to 360° to capture many independent speckle realizations. Each set of images at a particular axial rotation angle involved 20 image captures, the results being averaged together to reduce shot noise. Following speckle measurement, the mean irradiance on target was estimated by averaging 400 images taken as the target was rotated continuously to randomize the speckle. This mean irradiance estimate was used to normalize the speckle measurements on a pixel-by-pixel basis, thus mitigating the effects of irradiance and detector non-uniformity. Of note, a separate dark image was captured and used for the mean irradiance data set, as dark current noise does change slowly over time. Thus, the experimental procedure consisted of careful setup, coherence measurement, speckle measurement, and mean irradiance estimation.

IV. Results

The results from the experiment measurements were compared to theory for speckle contrast, speckle irradiance probability density function (PDF), and speckle size. As will be shown, all comparisons of experimental data with theory are good, while the speckle contrast comparisons agree very well. From these results, Hu's model and the modified Huntley model are found to be valid, at least for the range of conditions studied here.

4.1 Speckle Contrast

After the experimental procedure was complete, post-processing was straight-forward. Within the FWHM mean irradiance masked region, any pixel values below zero (due to dark image subtraction) were truncated to 0, though this truncation was never observed to change the computed contrast by more than 0.1%. The final data set for a particular slope angle included all 12 sets of speckle measurements, totaling about 1,800 independent speckle samples. Using that data, the mean and standard deviation of the normalized speckle irradiance were computed, leading to the speckle contrast value, which is simply the standard deviation divided by the mean.

Figure 4.1 shows the comparison of measured speckle contrast with standard error bounds to both Hu's more exact theory and the computationally efficient Huntley equations, both in original and modified versions. The widths of the error bounds represent uncertainty in the measured slope angle. Figure 4.2 shows the same comparison, but with single measurement uncertainty shown instead of error bounds.

Comparing the data to Hu's theory, excellent agreement is observed. The same can be said for the Huntley equations, both original and modified. The modified Huntley curve plotted here assumes a Lorentzian source distribution, which reasonably approximates the true distribution (see Figure 3.12), as well as a coefficient of 1.749, which was found to minimize squared error between the Hu and modified Huntley models over a wide range of tactically relevant conditions, as will be discussed in more depth later.

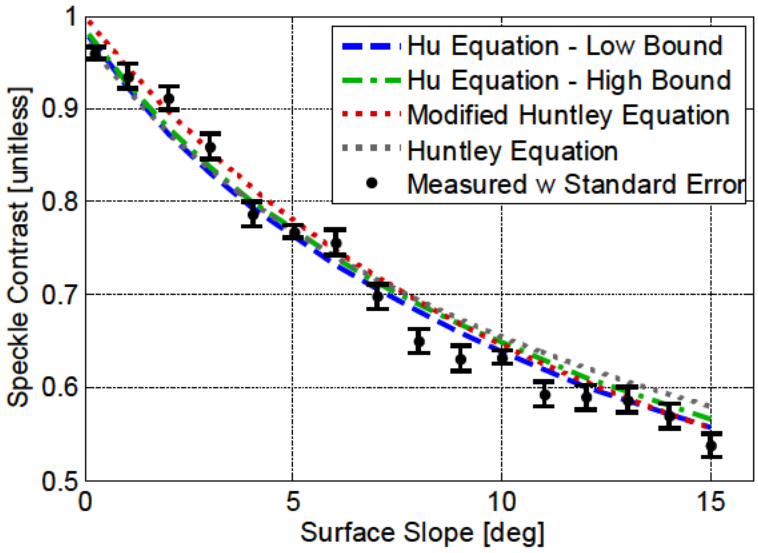

Figure 4.1. A comparison of measured speckle contrast with both Hu and Huntley theory. Solid agreement is observed between all three. Some discrepancies between Hu's more exact theory and the computationally-efficient modified Huntley theory are observed, but these differences are small with mean difference of 1.4% and difference standard deviation of 1.0%. The measured data also shows some small disagreements with Hu's theory with -1.1% mean difference and 2.9% standard deviation.

The shortcomings of the original Huntley equation begin to become evident around 0.6 speckle contrast. At that point, the original Huntley predicts higher values than the other equations or the measurements, a trend which continues as contrast drops

further, as will be shown later. Further, some discrepancies between the Huntley equations, the Hu equation, and the data are visible. To quantify the differences, taking the Hu equation as truth, the modified Huntley equation had mean error of 1.4% and standard deviation of error of 1.0% over the region shown, while the measured data had -1.1% mean error and 2.9% standard deviation. Thus, the measured data and both models all agree well, leading to the conclusion that the theory is valid over the contrast range of about 0.55 to 1.

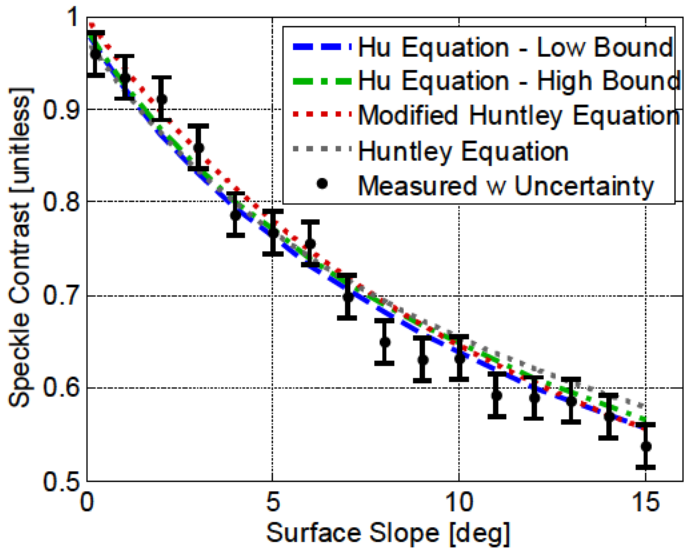

Figure 4.2. A comparison of the measured speckle contrast to both Hu and Huntley theory. In this plot, single measurement uncertainty is shown instead of standard error bounds.

The vertical error bounds on the data in Figure 4.1 were computed from experimental measurement variation based on the definition of the standard error of the mean. The standard error of the mean, *SEM*, is given by

$$SEM = \sigma / \sqrt{N} \tag{32}$$

where σ is the standard deviation of the measurements (shown in Figure 4.2) and N is the sample size. The SEM defines the range over which 68% of measurements should fall. Its use requires that the error be unbiased and normally distributed. Figure 4.3 shows that the error distribution is very roughly normally distributed (based on only 32 samples), supporting use of standard error here, though true justification would require a much larger sample set. Of note, the -1.8% bias due to only 4.8 samples per speckle radius was removed previously such that the speckle contrast measurements are also expected to be unbiased, an assumption which is justified by the solid match between experimental data and Hu's theory with mean difference of only -1.1%. With the understanding that *SEM* is appropriate for use here, the vertical error bounds shown in Figure 4.1 define the approximate range over which 68% of mean estimates should fall if this experiment were repeated an infinite number of times. Phrased differently, the plotted vertical error bounds show the approximate 68% confidence intervals. The plot shows that 11 of 16 or 68.75% of the bounds do include the Hu curve, a fact which supports the conclusion that Hu's theory is valid.

The standard error bounds are largely constant over the range of surface slopes shown, indicating that measurements could have been taken at even higher slope angles. However, the speckle contrast was measured prior to measuring the true laser PSD. At that point, a Gaussian source distribution was assumed, causing the data to break away from the theoretical curve at about 10° slope. However, it was assumed at that time that dark noise was the cause of the break-away, and thus, data was only taken out to 15° slope.

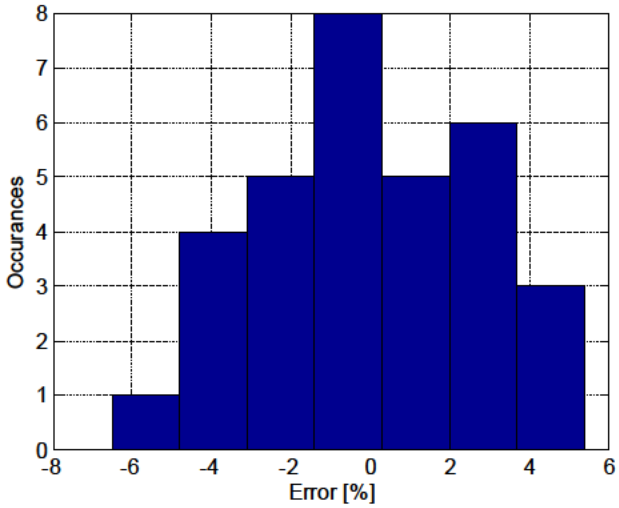

Figure 4.3. An example of the speckle contrast measurement error distribution employing 32 speckle contrast measurements. Note that the distribution of error can very roughly be taken as normally distributed.

Two other error bounds are also shown in Figure 4.1. First, the horizontal width of the error bounds on the measurements represents the slope angle uncertainty. These error bounds are uniform from one angle to the next at +/- 0.25°, the approximate resolution of the rotation plate. Lastly, two Hu theory curves are plotted, one for the upper bound and one for the lower bound. These bounds are based on uncertainty in three other measured parameters which are used as inputs to the Hu equation, namely peak wavelength, imaging aperture diameter, and object distance.

The Huntley equation IFOV coefficient value of 1.749 was chosen to minimize squared error between the modified Huntley equation and the Hu equation. The original Huntley equation was also fitted to Hu's theory, but a new curve fit was necessary due to the improvements made to the Huntley equation as a part of this work, and two detailed examples of this curve fit are shown in Figures 4.4 and 4.5. In Figure 4.4, a Gaussian

source spectrum is used with tactically relevant parameters (see the figure caption for details). The plot on the left shows a direct comparison between Hu's theory and the modified Huntley equation, and agreement is excellent for the overall least squared error IFOV coefficient of 1.749. On the right, the difference between the two is shown. This difference peaks near unity contrast (zero slope), where it appears that the geometrical approximations break down to some extent. Error is 0.8% mean and 1.8% standard deviation. One might ask whether the fact that the Hu theory accounts for speckle reduction due to surface roughness while the modified Huntley equation does not has any impact on this curve fitting. That fact does not have any impact, as the surface roughness of only 3.27 μm standard deviation, much smaller than the coherence length of 1 mm, reduces speckle contrast by an insignificant amount. This figure also shows the original Huntley equation results, which differ significantly from the Hu theory below about 0.5 contrast.

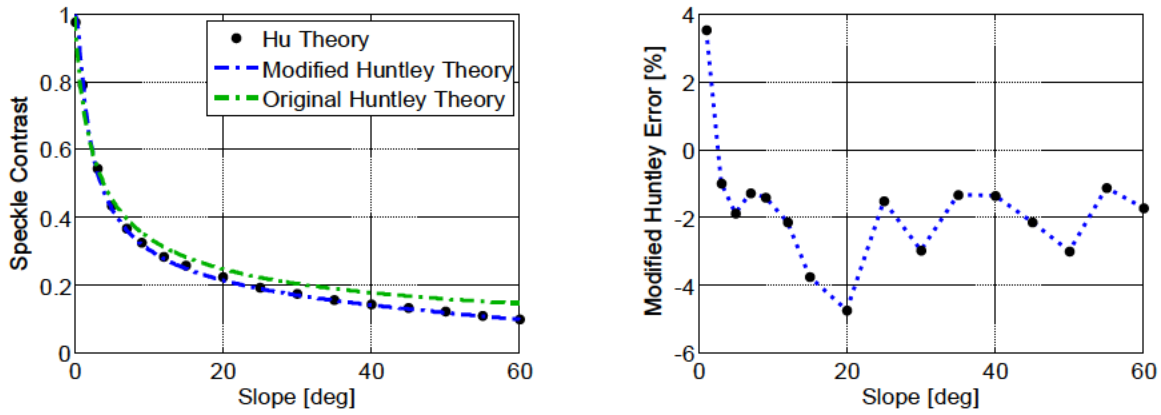

Figure 4.4. Fitting the modified Huntley equation to Hu's more exact equation. The plot on the left shows the LSE comparison of the two equations, along with the original Huntley equation, while the plot on the right shows the modified Huntley equation error. Note that the greatest error occurs near unity contrast

(zero slope). The source PSD here is Gaussian. Parameters: 0.3 m aperture diameter, 5 km range, 1 μm wavelength, and 1 mm coherence length.

Figure 4.5 shows much the same data for a Lorentzian source spectrum. Once again, the highest error occurs near unity contrast, while the total error is 1.5% mean and 2.3% standard deviation. Also of note, a modern Intel i7-4770 CPU took about 16 hours to generate the Hu theory data used in these curve fits, while it took only about 20 milliseconds to generate the Huntley curves at about 30 times higher resolution, illustrating the numerical advantage of the Huntley equation for direct calculations.

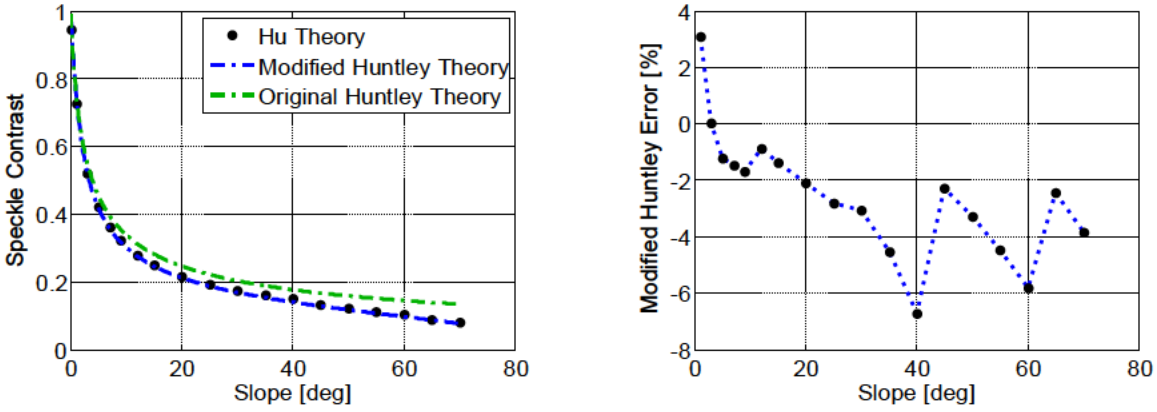

Figure 4.5. Fitting the modified Huntley equation to the Hu equation for a Lorentzian source distribution. Once again, the left plot shows a direct comparison of the two, along with the original Huntley equation, while the right plot shows the modified Huntley error. Also as before, the largest error occurs near unity contrast. Parameters: 0.3 m aperture diameter, 5 km range, 1 μm wavelength, and 1 mm coherence length.

The final value for IFOV coefficient of 1.749 involved 24 curve fits over a wide range of parameters relevant to tactical tracking. Tables 4.1 and 4.2 summarize the curve

fits for Gaussian and Lorentzian source spectrums respectively. Both used the same set of parameters including aperture diameters of 0.3 to 1.0 m, object distances of 500 to 20,000 m, wavelengths of 1 and 1.5 μm, and coherence lengths of 0.1 to 2 mm (not including the experiment parameters, which fell well outside those ranges). The shown best-fit coefficients produced the smallest squared error for each parameter set and ranged from 1.677 to 1.868. The chosen IFOV coefficient of 1.749 was the mean of these best-fit coefficients. The mean error percentages are shown for both the best-fit for each parameter set and the best overall fit. Using the best overall fit coefficient of 1.749, the mean error of the modified Huntley equation was 0.37% while the standard deviation was 2.02%. Thus, using an IFOV coefficient of 1.749 produced low error over the wide range of conditions tested.

Table 4.1. Data summarizing the curve fit of Huntley's equation to Hu's theory for a Gaussian spectrum.

Aperture Dia. (m)	0.3	0.3	0.3	0.6	0.6	1.0	1.0	1.0	1.0	1.0	1.0	2.72 mm
Object Dist. (m)	500	500	5 km	10 km	20 km	500	500	500	500	5 km	10 km	2.934
Wavelength (μm)	1.000	1.500	1.000	1.000	1.000	1.000	1.500	1.000	1.500	1.500	1.500	0.671
Coh. Lgth. (mm)	0.100	1.000	1.000	1.000	2.000	0.100	0.100	1.000	1.000	0.500	1.000	0.259
Best-Fit Coeff.	1.709	1.777	1.706	1.706	1.706	1.777	1.768	1.866	1.822	1.726	1.726	1.776
Best Mean Error %	0.345	0.715	0.252	0.252	0.252	0.637	0.543	1.604	1.454	0.282	0.272	0.646
Best Std Error %	1.946	2.185	1.646	1.646	1.646	2.167	2.069	2.725	2.758	1.731	1.727	2.056
Mean Error %	-0.632	1.323	-0.802	-0.802	-0.802	1.323	1.047	2.904	2.469	-0.253	-0.263	1.248
Std Error %	2.143	1.982	1.829	1.829	1.829	1.957	1.931	2.032	2.231	1.824	1.820	1.864

Table 4.2. Data summarizing the curve fit of Huntley's equation to Hu's theory for a Lorentzian spectrum.

Aperture Dia. (m)	0.3	0.3	0.3	0.6	0.6	1.0	1.0	1.0	1.0	1.0	1.0	2.72 mm
Object Dist. (m)	500	500	5 km	10 km	20 km	500	500	500	500	5 km	10 km	2.934
Wavelength (μm)	1.000	1.500	1.000	1.000	1.000	1.000	1.500	1.000	1.500	1.500	1.500	0.671
Coh. Lgth. (mm)	0.100	1.000	1.000	1.000	2.000	0.100	0.100	1.000	1.000	0.500	1.000	0.259
Best-Fit Coeff.	1.679	1.778	1.677	1.677	1.677	1.774	1.763	1.868	1.830	1.702	1.702	1.774
Best Mean Error %	0.532	0.592	0.266	0.266	0.263	0.875	0.706	1.108	1.019	0.307	0.298	0.608
Best Std Error %	2.689	1.768	2.045	2.045	2.042	2.662	2.418	2.062	2.106	1.976	1.961	1.731
Mean Error %	-1.217	1.217	-1.535	-1.535	-1.538	1.487	1.087	2.556	2.201	-0.839	-0.848	1.164
Std. Error %	3.060	1.554	2.327	2.327	2.322	2.453	2.300	1.353	1.550	2.176	2.155	1.530

4.2 Speckle Irradiance PDF

To compare theoretical to experimental PDFs, the entire data sets for a particular slope angle were used to form histograms, which, after normalization to integrate to unity, represent the measured irradiance PDFs. Those PDFs can then be compared to the approximate gamma PDFs based on *N* from the modified Huntley approximation, as discussed in Section 2.4. Such comparisons are shown in Figures 4.6 to 4.9. In Figure 4.6, the measured PDFs for very low slope angles (0° and 2°) peak slighter higher and to the right of the approximate theoretical distributions. Figure 4.7 shows slopes of 4° and 6°, for which the data again peaks higher and to the right of the theory. In Figure 4.8, the peak placements are about collocated, but once again the measured data shows lower probability of near zero irradiance and higher peak probability than predicted. Figure 4.9 shows much the same result for the highest slopes of 12° and 14°. Thus, while the Huntley approximation matches the speckle contrast well, the Gamma approximation for

PDF based on the Huntley approximation does not match the data nearly as well. The distributions appear to be fundamentally different. Some of this difference can be explained by the fact that shot noise, which has a non-zero-mean Gaussian distribution, tends to blur the measured PDF and shift it rightward, but that factor cannot explain why the measured irradiance peaks higher than predicted by theory. It is unfortunate that exact PDF models are not available in the literature for comparison.

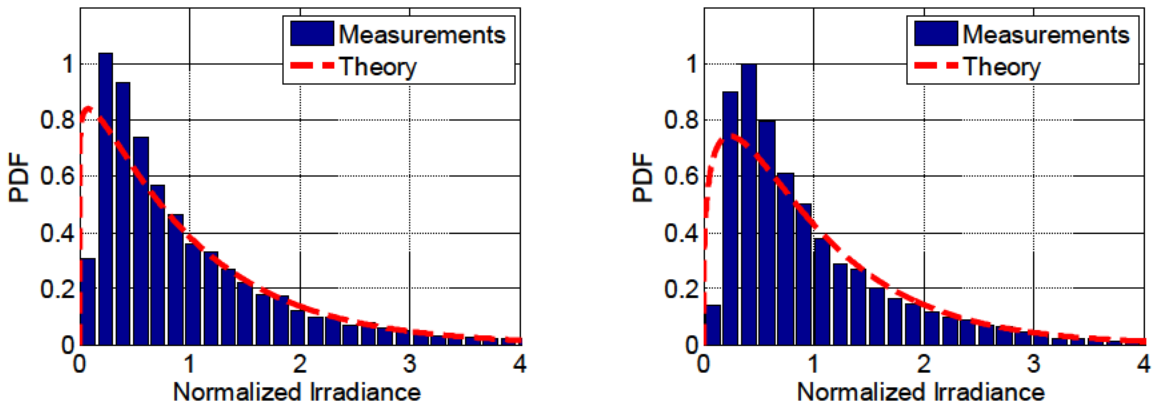

Figure 4.6. Experimental and theoretical speckle irradiance PDF comparisons for surface slope of 0° and 2°. Decent agreement is seen between theory and measurement, but there are considerable differences. Namely, for these very low slope angles, the measured PDFs peak higher and to the right of the theory.

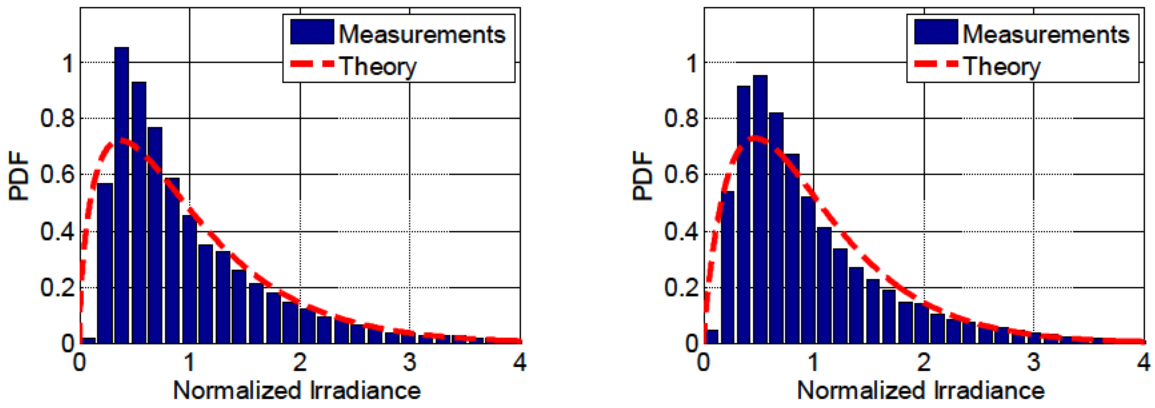

Figure 4.7. Experimental and theoretical speckle irradiance PDF comparisons for slopes of 4° and 6°. Once again, the experimental PDFs peak higher and to the right of the theoretical ones.

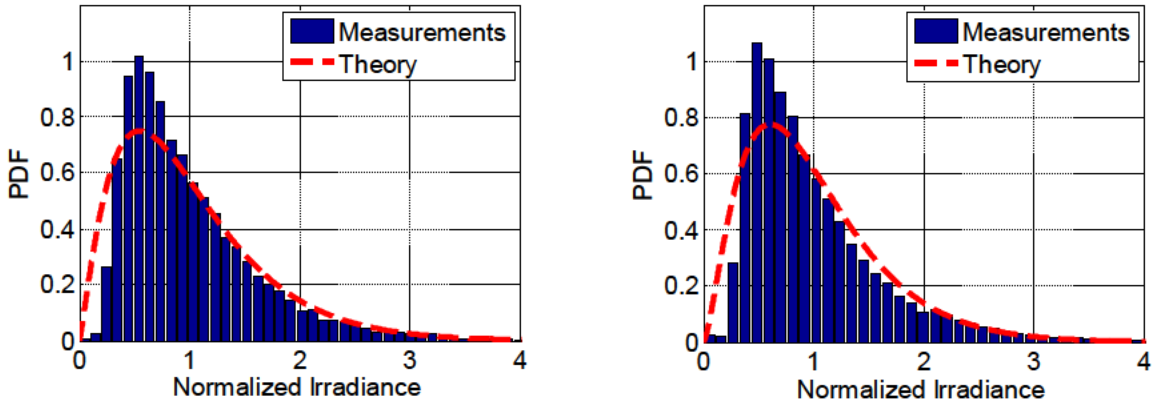

Figure 4.8. Experimental and theoretical speckle irradiance PDF comparisons for slopes of 8° and 10°. The experiment PDFs now peak close to the irradiance levels of the theoretical peaks, though the distributions are still clearly different.

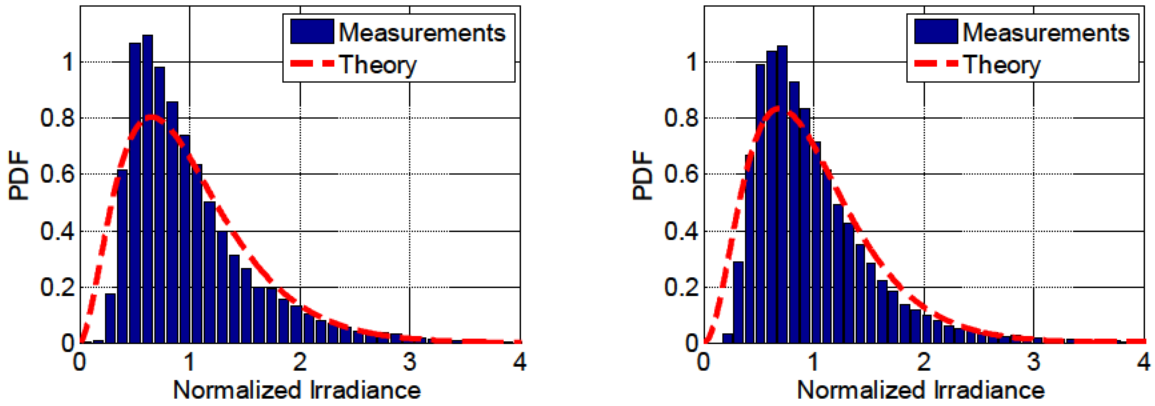

Figure 4.9. Experimental and theoretical speckle irradiance PDF comparisons for slopes of 12° and 14°. Now, the experimental peak might be slightly to the left of the theory. The experimental PDFs still peak to higher values.

4.3 Speckle Size

In Section 2.5, the theory regarding speckle size was established. A comparison of the experimental results to that theory is worthwhile to better establish the credibility of the results and to check for anything unexpected. Such a comparison is shown in Figure 4.10. Here, decent agreement is observed between the data and the theory, though notable

differences exist for shifts between 1 and 3 pixels. Of note, the combined data from all slope angles indicates that 1/e speckle width is about 12% smaller than predicted by theory.

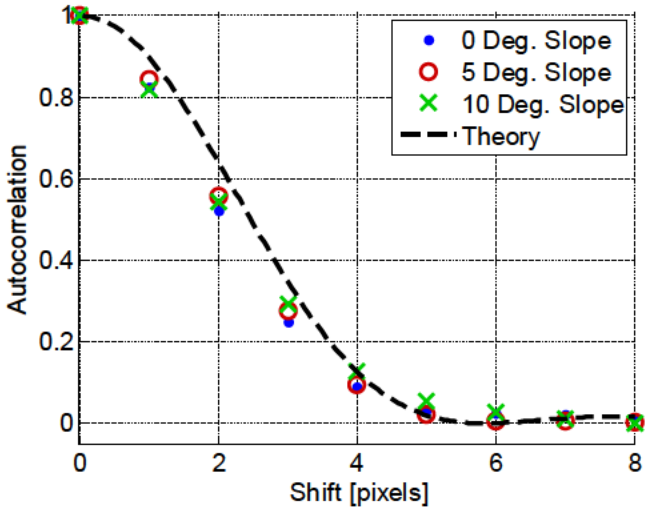

Figure 4.10. A comparison of measured speckle size (autocorrelation) to the established theory. Decent agreement is shown, but differences exist, especially over the range of 1 to 3 pixel shifts. The 1/e point falls in this range, and the measured 1/e speckle width for all slope angles combined is 12% narrower than predicted by the theory.

The autocorrelation based on experimental data was computed by first windowing the normalized speckle images using a square window over a region of mean irradiance always greater than half its maximum value. Next, the Weiner –Khinchin theorem was used to estimate the autocorrelation, ρ, according to

$$\rho = F^{-1}\{F\{I_s\}F\{I_s\}^*\} \tag{33}$$

where F is the Fourier transform and I_s is the measured speckle irradiance. After that, the estimated autocorrelation from each speckle measurement was averaged together.

As was noted previously, it appears that speckle observed during the experiment was narrower than expected from theory. A numerical simulation was also run with 4.8 pixels/speckle to investigate whether the sampling may have caused the difference, but that does not appear to be the case. Rather, either noise, small speckle image size, uncertainty in experimental parameters, or some combination of the three must be the cause. Even if the speckle width truly is 4.24 pixels, the only major change in speckle contrast findings would be due to a change in the 1.8% correction factor for constant speckle contrast error due to few pixels per speckle. That factor would become 2.3%, resulting in -0.6% mean difference between the measurements and Hu's theory instead of the presented -1.1% mean difference. Such a change would not alter the conclusion that the Hu theory is validated by this experiment, so no further investigation into true speckle size was done.

Also of note, the speckle size does not appear to change with slope angle. This observation agrees with the current understanding of speckle. Recall from Section 2.5 that speckle size is dependent only on wavelength, aperture diameter, and distance between the aperture and the detector. Thus, surface slope and the associated degrees of freedom should not impact speckle size. While a tiny increase in size with slope is visible in Figure 4.10, this increase could easily be due to noise, as the observed autocorrelation was not always higher for higher slope, but rather there was dependence on the exact pixel shift, indicating that the apparent tiny increase in size with slope angle was in the measurement noise.

Thus, while observed speckle size was narrower than expected from theory, the validation of the speckle contrast theory was not impacted. Further, speckle size did not increase with slope, as predicted by theory.

V. Conclusion

5.1 Summary

In this work, the statistical properties of speckle relevant to tactical HEL active illumination were investigated with a focus on rapid numerical modeling to address a current need to simulate such systems for system design, target recognition, aimpoint identification, and tracking algorithm development. Equations were presented for the statistics of fully developed speckle as well as the reduction in speckle contrast due to polarization diversity, target roughness, and target slope. Further, theory was shown regarding the size of speckles and the approximate PDF of reduced contrast speckle. For active illumination, speckle contrast reduction is often dominated by the interaction of the short coherence length of the source and the slope of the target surface, while other factors generally reduce speckle contrast by less than a factor of two. Because the most exact equation available for sloped surface speckle, developed by Hu, does not have a known closed-form solution, a simpler equation, the modified Huntley equation, was also developed. This equation uses geometrical approximations. It also includes a previously derived correction factor to improve accuracy over the original Huntley expression. By minimizing squared error compared to Hu's equation, the modified Huntley IFOV coefficient was found to be 1.749, and agreement between the models was solid with 0.4% mean error and 2.0% standard deviation over a wide range of tactically relevant conditions. The Huntley approximations also allowed the use of a closed-form approximation for speckle irradiance PDF involving the Gamma distribution. The final

theoretical mention was the well-known equation for speckle size with a circular imaging aperture.

With the theory defined, an experiment was designed to validate the sloped target speckle theory. Many competing factors were balanced. The initial design carefully balanced and controlled speckle spatial sampling, number of speckles captured, pixel IFOV on target (and number of rough surface features sampled), detector dark current and shot noises, laser coherence area on target, and laser coherence length. Many sources were tested, and the Toshiba T0LD9200 laser diode was finally selected for its short coherence length. Even with this source, obtaining the short coherence length necessary to observe reduction in speckle due to target slope under laboratory space constraints required that power be limited to about 3.5 mW. Further, ensuring that the illumination coherence area was greater than the IFOV was found to be insufficient for this source, as fairly small, but unacceptable, levels of illumination nonuniformity were still present in each IFOV. Thus, further expansion of the beam such that the minimum diffraction-limited spatial period ($\lambda R/D$) was about three times the IFOV was necessary, further reducing irradiance on target. Irradiance on target was low enough that even after periodic correction for dark current noise and averaging twenty speckle measurements together to reduce shot noise, speckle measurement beyond about 15° slope, or speckle contrast of about 0.55, was not attempted due to excessive noise. Even so, useful measurements were taken up to 15° slope.

Comparison of the experimental results with theory validated the contrast reduction models, agreed fairly well with speckle size theory, and showed considerable disagreement with the approximate PDF model over the range of conditions tested.

Comparing Hu's theory for contrast reduction due to slope to the experimental measurements showed excellent agreement with 11 out of 16 of the experimental 68% confidence interval bounds encompassing the theoretical curve. The difference between Hu's theory and measurements had a mean of -1.1% and standard deviation of 2.9%. Some disagreement between the Hu and Huntley equations was also observed, especially near unity speckle contrast where the geometrical approximations appear to break down to some extent. Still, the disagreement was small with mean difference of 1.4% and standard deviation of 1.0%, indicating that the Huntley equation's numerical efficiency should justify its use in many cases. These results indicate that both models, modified Huntley and Hu, are valid, at least over the range of speckle contrast test here. The measured speckle size was also in decent agreement with established theory, though measured speckle size was somewhat smaller than predicted by continuous theory. Ultimately, that difference had no impact on model validation conclusions. Also, as expected, speckle size did not appear to change with slope angle. Further, the measured speckle irradiance PDFs differed rather significantly from the theoretical PDFs based on the geometrical approximations of the Huntley model, with higher and narrower observed peaks than were predicted.

5.2 Future Work

Future research can build on this work in several areas including incorporation of the new sloped surface speckle model into simulation packages, development of target and aimpoint ID algorithms based on this speckle model, extension of sloped target speckle contrast validation out to lower contrast levels, and development of an exact

speckle irradiance PDF model for comparison with measurements. Regarding HEL tracking modeling, numerical simulation software such as the High Energy Laser System End to End Model (HELSEEM) and Physics-based Imaging and Tracking of Ballistics, UAVs, and LEO Satellites (PITBUL) are used during the initial phase of HEL system design to determine what tracking hardware is necessary to meet performance requirements. With the incorporation of the modified Huntley model into these simulation packages, they will provide more accurate results regarding active tracking performance. Increased accuracy will lead to better hardware and cost estimates from the initial design phase. Further, more accurate active tracking simulations will allow better evaluation and tuning of tracking algorithms prior to physical testing. This modeling improvement will reduce the time and cost required during the field test phase by providing better performance estimates prior to field tests during the inexpensive simulation phase.

Additionally, new target recognition and aimpoint ID algorithms can be developed to exploit the target information included in speckle imagery. The target's surface slope has a large impact on speckle contrast. Further, for a moving platform and/or target, speckle usually decorrelates quickly over time, providing many independent speckle images in a fraction of a second. Thus, by first using a short time sequence of speckle images to estimate speckle contrast across the target (see Figure 5.1), surface slope across the target can then be computed using the modified Huntley equation. The speed and accuracy of the new speckle model could allow this computation to be done in real time during military operations. From slope, a three-dimensional model of the portion of the target visible to the camera could be constructed to aid in target

recognition. Alternatively, the slope could be used to identify aimpoints on the target by looking for abrupt changes, such as often occur at the vulnerable wing joint of an aircraft where the slopes of the wing and of the body often differ significantly.

Figure 5.1 shows an example of speckle contrast estimation using 0.25 seconds of speckle video. From this figure, it is clear that some image processing might be needed to reduce noise. Even so, some interesting features are clearly visible, including peaks in speckle contrast on the nose cone and turret ball, where slope angle drops close to zero. Surface slope near zero is desired for optimal coupling of HEL energy into the target surface, so both of those points could be useful aimpoints. Another interesting feature is the dip in contrast at the wing joint, which is also a potential aimpoint. Some initial research has already shown promise for this type of aimpoint ID [Van Zandt, 2014]. Thus, the modified Huntley equation could allow development of new target and aimpoint ID algorithms for field use.

As another area for future research, additional model validation out to lower contrast levels could be accomplished in one of two ways. First, dark current noise can be further reduced by implementing a fast electronic shutter to allow near instantaneous capture of both dark images and speckle images. Such a method allows a separate dark current image for each speckle image. The range of contrast measurement could be extended modestly, ultimately being limited by shot noise, which introduces a bias in measured irradiance as shot noise becomes very large. That bias could theoretically be removed by deconvolution of the measured PDF with the blur function due to shot noise, though deconvolution of noisy signals is challenging. Eventually, some noise floor will be reached which cannot be overcome by current techniques. The second option to extend

contrast measurement range is to use a laser designed to have both short coherence length and high output power. For example, the Toptica iBeam SMART 640 offers 150 mW of power with coherence length around 100 µm, but was outside the budgeted range of this work. Such a laser would increase SNR and allow a considerable increase in measurement range, probably to below 0.2 contrast.

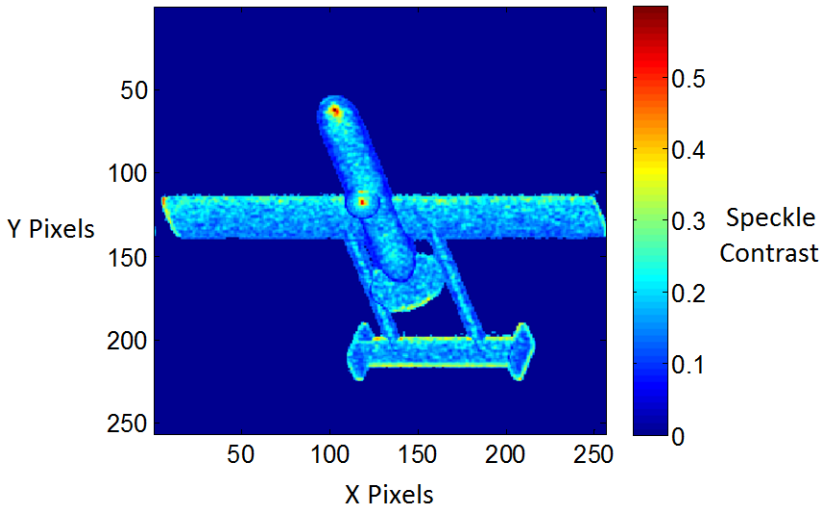

Figure 5.1. Estimate of speckle contrast across a UAV target from 250 milliseconds of simulated active illumination video. Notable features include a dip in speckle contrast at the wing joint and peaks on the nose cone and turret ball where surface slope drops close to zero. PITBUL was used for the simulation.

Another possibility for future work is the development of more exact theory for sloped target speckle irradiance PDF. The comparisons of measured PDFs with the approximate model showed considerable discrepancies. Thus, the development of a sloped surface speckle PDF model which does not rely on as many approximations would be valuable progress.

Appendix A – Numerical Modeling of Speckle Video

Simulating time sequences of speckled imagery in the presence of multiple speckle reduction factors is challenging. Numerical simulation requires as short a computation time as possible so that even very large studies can be completed in a reasonable timeframe. Additionally, a good degree of accuracy is required such that the results are broadly relevant. With these goals in mind, a rapid simulation approach was developed which uses a weighted sum of fully speckled field amplitude and unspeckled field amplitude in the image plane. The weighting is computed such that speckle contrast exactly matches the value computed using the multiple effect speckle reduction method of Section 2.3, which utilizes the modified Huntley equation developed in Section 2.2. Higher-order statistics differ somewhat, but overall accuracy is found to be acceptable for a numeric model, and computation time is short. Further, numerical methods for simulating aperture and turbulence blurring and time decorrelation of the speckle field due to platform and/or target motion are briefly discussed.

A.1 Speckle Image Generation

As discussed in Section 2.2, three speckle reduction factors come into play for tactical active tracking, polarization diversity, surface roughness, and surface slope. In that section, equations yielding speckle contrast due to each of those effects individually were presented. In Section 2.3, an equation which combines all effects to produce a single speckle contrast value was given. That equation can be used on a pixel-by-pixel basis to compute a speckle contrast image of the target for numerical simulation.

However, this speckle contrast image only defines the first-order statistics. In order to create simulated imagery, random draws must be taken from these statistics. One particularly fast method to do so is through a weighted sum of an unspeckled (or incoherent) field and a random fully speckled (or fully coherent) field. Note that field amplitude, not irradiance, is used for the weighted sum. Goodman reviews the statistics of such an operation and finds that the speckle contrast is given by

$$C = \frac{\sqrt{1+2r}}{1+r} \tag{A.1}$$

where r is the ratio of the unspeckled irradiance over the mean fully speckled irradiance [Goodman, 2007:30-34]. After some math, the fractional component of the total irradiance contributed by the unspeckled component, I_0, is given by

$$I_0 = 1 - \frac{1}{N_{total} + \sqrt{N_{total}\left(N_{total}-1\right)}} \tag{A.2}$$

where N_{total} is the total number of degrees of freedom due to all speckle reduction effects. Of course, the fractional component contributed by the random fully speckled irradiance, $\langle I_n \rangle$, is then given by

$$\langle I_n \rangle = 1 - I_0 = \frac{1}{N_{total} + \sqrt{N_{total}\left(N_{total}-1\right)}} \tag{A.3}$$

The final irradiance, I, is then given by

$$I = \left(\sqrt{I_0}A_{unspeckled} + \sqrt{\langle I_n \rangle}A_{speckled}\right)^2 \tag{A.4}$$

where $A_{unspeckled}$ is the unspeckled field amplitude, and $A_{speckled}$ is the fully speckle field amplitude. This equation is applied pixel-by-pixel across the entire image.

By using this weighted sum method, the irradiance PDF is approximated as a modified Rician, as opposed to the usual approximation as Gamma [Goodman, 2007:31]. However, the Gamma approximation is just that, an approximation, and one which the modified Rician matches quite well, as shown in Figure A.1. The two PDFs match nearly exactly for both low and high numbers of degrees of freedom, N. However, for N between about 1 and 16, some noticeable differences exist. Even so, these differences are small enough to be tolerated in exchange for the associated reduction in run time that this method affords.

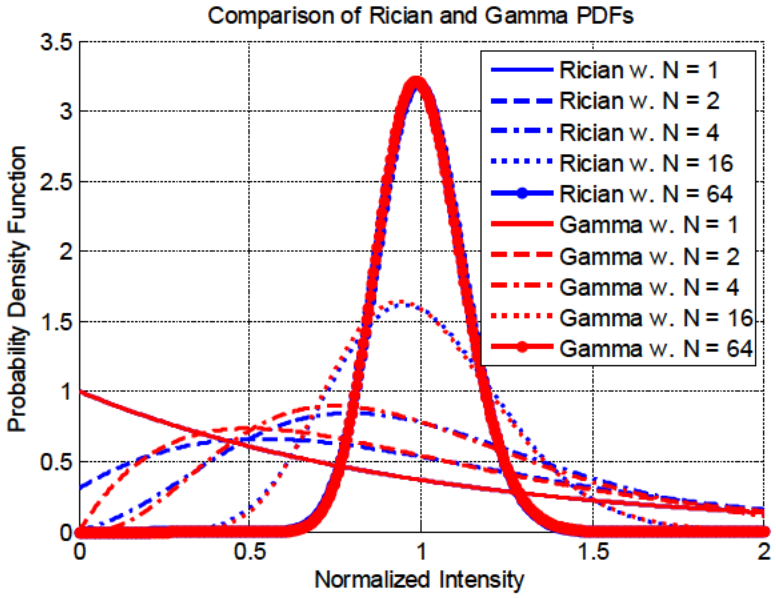

Figure A.1. A comparison of Rician and Gamma PDFs. The PDFs match nearly exactly for N=1 and N > 16, while for N between 1 and 16, some disagreement is visible.

The method used to generate the unspeckled (incoherent) and random fully speckled images (fully coherent) is also worth noting. Generation of both utilizes wave

optics simulation such that atmospheric turbulence is well-modeled. To be more specific, a wave optics package developed by MZA Associates called WaveTrain is employed. For fully coherent image generation, wave optics can be used directly, as wave optics is inherently fully coherent. The source field amplitude is created by taking the square root of the irradiance reflected from the target in the direction of the imaging aperture. The source field phase is initialized to uniformly-distributed random numbers in the range [0, 2π], which was previously noted to be the condition for fully-developed speckle. In other words, each pixel is given a random phase to represent the randomly rough target surface. The complete source field is then propagated through a series of phase screens which apply random phase distortions appropriate to the level of turbulence present in each path segment. Thus, atmospheric turbulence effects are well-modeled. The field arriving at the imaging aperture is recorded as the fully speckled field.

Because wave optics is inherently fully coherent, for the incoherent or unspeckled image, the "Light Tunneling" technique is used [Praus II, 2007]. This technique propagates a grid of point sources located at the target's location to the imaging aperture. The light which arrives from each point source is analyzed to compute the tilt and blur caused by atmospheric turbulence for light originating at that location. Thus, by analyzing all of the point sources across the target grid, the spatially and temporally varying effects of turbulence are computed. Those effects are interpolated up to the full image resolution and applied to the image of the target [Praus II, 2007]. Thus, while wave optics is used directly for fully speckled image generation, "Light Tunneling" allows the application of wave optics turbulence tilt and blur to incoherent images as well.

The effects of diffraction or aperture blurring are also applied to the images. These effects are applied in the frequency domain via the optical transfer function (OTF) for the unspeckled or incoherent images and the amplitude transfer function (ATF) for the speckled or coherent images. Thus, both turbulence and aperture effects are applied prior to the weighted sum operation which creates partially speckled images.

A.2 Time Decorrelation Due to Motion

One other major effect comes into play during speckle video simulation, namely time decorrelation of the speckle due to platform and/or target motion. Because the target and/or platform are often moving during HEL engagements, the effective surface slope is constantly changing. Because optical wavelengths are usually only about 1 μm, very small changes in surface slope can completely decorrelate the speckle pattern in the image plane. Consider that when illuminating light reflects off of the target's rough surface, a speckle field is created across the entire hemisphere centered about the target's surface normal, as some light from each point on the target's surface is reflected to all parts of that hemisphere. The distant imaging aperture receives only a very small portion of the total reflection, creating a speckle field across it. That unique speckle field across the aperture then produces a unique speckle field in the image plane. To consider the impact of changing target slope, recall the Fourier optics axiom that tilt (slope) in the near field produces displacement in the far field. Thus, as the target slope changes over time, the hemispherical speckle field is displaced, eventually causing a completely new portion of the hemispherical speckle field to fall across the aperture. When this occurs, the

speckles in the image, which are dependent upon the speckles across the aperture, become totally independent of their previous state.

To model this in numerical simulation, a time-varying tilt is added to the phase of the light reflected from the target. The rate of tilt change depends upon the dynamic engagement. The faster the target and/or platform are moving, the faster the target surface slope changes. Wave optics then produces an appropriate decorrelation of the image speckle over time, properly representing the physics of the engagement for speckle video creation.

Using the methods discussed in this appendix, it is possible to create time sequences of speckled target images which include spatially and temporally varying turbulence effects, aperture blurring, and speckle decorrelation due to motion. An example of one image from such a time sequence is shown in the left of Figure A.2. Here, a small UAV is laser illuminated, causing some speckle across the image. The changes in speckle contrast across the target can be difficult to distinguish. Thus, the right side of the figure shows computed speckle contrast using 250 ms of speckle video of the moving target. From this figure, it is clear that speckle contrast does change across the target. This fact highlights the potential utility of speckle decorrelation over time due to relative motion and the need to model such effects accurately. Most prominently, speckle contrast peaks over the nose cone and turret of the UAV, where surface slope drops down close to 0. Also, contrast drops near the wing joint of the UAV, where the slope of the body of the UAV increases to meet the wing at about a 90° angle. Thus, images generated using the method described here include turbulence, aperture, and relative motion effects, and we

have seen an example of the information present due to the speckle decorrelation caused by relative motion, highlighting the importance of accurate modeling of such effects.

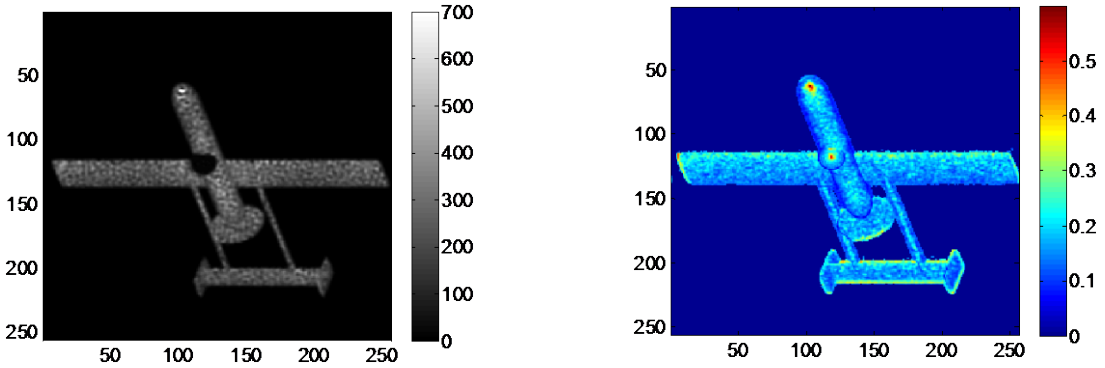

Figure A.2. A simulated image of a small UAV under laser illumination. The left side shows an example image, while the right side shows estimated speckle contrast computed using 250 ms of speckle video. In the figure on the left, some speckle is clearly present, though it is reduced by the short coherence length of the illuminator and the slope of the target. On the right, it becomes more clear that speckle contrast does change significantly across the target due to changes in surface slope.

Appendix B – Matlab Code

B.1 numberOfSamplesRequired.m

```
% For N coherence areas, the speckle intensity will follow a Gamma
% distribution with shape parameter, A, equal to N and scale parameter,
B,
% equal to I0, which is equal to I/N, where I is the mean intensity.
% However, Matlab's built-in Gamma function does not exactly follow
% Goodman's definition, so the first section's results are only
approximate.
% In the second section, speckle fields are created by propagating
randomly
% phased fields through apertures, yielding exact results.

clear; clc

%% Section 1 - Draws from a Gamma Distribution

% coherence area vector:
N = [1 2 3 4];

% Let mean intensity I equal 1:
I = 1;
I0 = I./N;

% The speckle contrast is equal to 1/sqrt(N):
C = 1./sqrt(N);
% It is also equal to the intensity standard deviation over the mean:
sigma = I.*C;

samples = 448;     % the number of speckle samples acquired
setsOfSamples = 4000;   % the number of sets of samples for error
statistic computation
R = zeros(length(N), samples, setsOfSamples);
stdDevOfStd = zeros(length(N), 1);
stdDevOfMean = zeros(length(N), 1);
stdDevOfContrast = zeros(length(N), 1);
contrast = zeros(length(N), 1);
tic;
for i = 1:length(N)
    A = N(i);
    B = I./N(i);
    R(i, :, :) = gamrnd(A, B, samples, setsOfSamples);
    stdDevOfMean(i) = std(mean(R(i, :, :)));
    stdDevOfStd(i) = std(std(R(i, :, :)));
    stdDevOfContrast(i) = std(std(R(i, :, :)) ./ mean(R(i, :, :)));
    contrast(i) = std(R(i, :)) / mean(R(i, :));
end
toc

errorBounds_percentage = stdDevOfContrast ./ contrast .* 100;

% Take-away(s):
% The largest error bound occurred for N = 1, one coherence area.
```

```
%% Section 2 - Propagation of Speckle Fields

% An alternate method is to propagate a digital speckle field and
analyze the
% results. This approach yields more accurate results due to the
% differences between Matlab's and Goodman's definitions of the Gamma
% distribution, which skewed the last section's results.

% imageSize = 138;     % 448 speckles per speckle field w 3.68
pixels/speckle
imageSize = 276;     % 1791 speckles per speckle field w 3.68
pixels/speckle
% speckle area is assumed to be about pi * (lambda/D/2)^2
samples = 1000;
numSpeckles = (imageSize/4)^2;
speckleIntensity = zeros([samples imageSize imageSize]);
x = (1:imageSize) - imageSize/2;
y = x;
[X Y] = meshgrid(x, y);
dist = sqrt(X.^2 + Y.^2);
for i = 1:samples
    surfacePhase = rand(imageSize);
    field = exp(1i*2*pi*surfacePhase);
    aperture = zeros(imageSize);
    aperture(dist < 0.5/3.68*imageSize) = 1;      % divide 0.5 by 3.68
to get 3.68 samples per speckle
    speckleIntensity(i,:,:) = abs( ifft2(aperture.*fft2(field)) ).^2;
end

% autocorrelation = xcorr2(squeeze(speckleIntensity(1,:,:)) -
mean(mean(speckleIntensity(1,:,:))));

meanInt = zeros(1, samples);
stdInt = zeros(1, samples);
contrastInt = zeros(1, samples);
for i = 1:samples
    meanInt(i) = mean(speckleIntensity(i, :));
    stdInt(i) = std(speckleIntensity(i,:));
    contrastInt(i) = stdInt(i)/meanInt(i);
end
stdOfMean = std(meanInt(:));
stdOfStd = std(stdInt(:));
% *** Key Value!
stdOfContrast = std(contrastInt(:));

% Take-away(s):
% These results disagree somewhat with the previous results. They
should be
% more accurate.
```

B.2 speckleSpatialSampling_testOfPixelAveraging.m

```
% This script measures the speckle contrast error introduced by a
% user-specified number of pixels per lambda/D.
```

```
clear; clc;
close all

imageSize = 2^13;

x = (1:imageSize) - imageSize/2;
y = x;
[X Y] = meshgrid(x, y);
dist = sqrt(X.^2 + Y.^2);

% Compute the speckle contrast of a well-sampled speckle pattern
speckleIntensity = zeros([imageSize imageSize]);
surfacePhase = rand(imageSize);
field = exp(1i*2*pi*surfacePhase);
aperture = zeros(imageSize);
aperture(dist < 0.5/32*imageSize) = 1;  % the divisor of 0.5 defines
the fraction of the total width used by the aperture
speckleIntensity = abs( ifft2(aperture.*fft2(field)) ).^2;
% Here, there are about 12 pixels per lambda/D*Z
combinedSpeckleIntensity = mean(speckleIntensity, 3);
meanInt = mean(combinedSpeckleIntensity(:));
stdInt = std(combinedSpeckleIntensity(:));
contrast_true = stdInt/meanInt;

% Now, downsample the speckle pattern by a factor of 4 and see how the
% computed contrast compares.
sample = 16;
speckleIntensity_downSample = zeros(imageSize/sample);
for i = 1:imageSize/sample
    for j = 1:imageSize/sample
        xRange = sample*(i-1) + (1:sample);
        yRange = sample*(j-1) + (1:sample);
        irrad = speckleIntensity(yRange, xRange);
        speckleIntensity_downSample(j, i) = mean(irrad(:));
    end
end
meanInt = mean(speckleIntensity_downSample(:));
stdInt = std(speckleIntensity_downSample(:));
contrast_sampled = stdInt/meanInt;

contrastError = (contrast_true -
contrast_sampled)/contrast_sampled*100;

% Contrast error was 10.5% for 2 samples, 2.61% for 4 samples per
speckle,
% 0.65% for 8 samples per speckle.
% Contrast error:
% [0.6413, 0.6347, 0.6342] - 8 pixels/speckle; 8192 image size; 0.5/128
aperture; 16 samples/pixel
% [0.6182, 0.6318] - 8 pixels/speckle; 4096 image size; 0.5/64
aperture; 8 samples/pixel
% [0.6104, 0.5879] - 8 pixels/speckle; 2048 image size; 0.5/32
aperture; 4 samples/pixel
% So, error reduces by half with each doubling of the samples/pixel.
% True sampling error due to 8 pixels/speckle should be about 0.651.
```

```
% The error in computed sampling error due to only 16 samples/pixel is
2.0%.
% [2.5585, 2.5676] - 4 pixels/speckle; 8192 image size; 0.5/64
aperture; 16 samples/pixel
% [10.3431, 10.2885, 10.3227] - 2 pixels/speckle; 8192 image size;
0.5/32 aperture; 16 samples/pixel
% [10.2202, 10.2139, 10.1560] - 2 pixels/speckle; 4096 image size;
0.5/16 aperture; 8 samples/pixel
% Now, the error due to 16 samples/pixel appears to be about 1.2%, but
that
% could be due to the more limited number of samples used here.

% For the experiment, there were
% 670.96e-9/0.00272*(0.046 + 1/(1/.2 - 1/2.934)) / (2*7.05e-6) = 4.7979
% pixels/speckle.
% Contrast error is therefore 2.60/(4.5597/4)^2 = 1.8071.


%% Now, it will be interesting to see if those errors change at all for
% different numbers of coherence areas per pixel.

% Compute the speckle contrast of a well-sampled speckle pattern
N = 2;  % number of coherence areas per speckle
speckleIntensity = zeros([imageSize imageSize N]);
for i = 1:N
    surfacePhase = rand(imageSize);
    field = exp(1i*2*pi*surfacePhase);
    aperture = zeros(imageSize);
    aperture(dist < 0.5/16*imageSize) = 1;
    speckleIntensity(:,:,i) = abs( ifft2(aperture.*fft2(field)) ).^2;
end
combinedSpeckleIntensity = mean(speckleIntensity, 3);
meanInt = mean(combinedSpeckleIntensity(:));
stdInt = std(combinedSpeckleIntensity(:));
contrast_true = stdInt/meanInt;

% Now, downsample the speckle pattern by a factor of 4 and see how the
% computed contrast compares.
sample = 4;
speckleIntensity_downSample = zeros(imageSize/sample);
for i = 1:imageSize/sample
    for j = 1:imageSize/sample
        xRange = sample*(i-1) + (1:sample);
        yRange = sample*(j-1) + (1:sample);
        speckleIntensity_downSample(j, i) =
mean(mean(combinedSpeckleIntensity(yRange, xRange)));
    end
end
meanInt = mean(speckleIntensity_downSample(:));
stdInt = std(speckleIntensity_downSample(:));
contrast_sampled = stdInt/meanInt;

contrastError = (contrast_true -
contrast_sampled)/contrast_sampled*100;

% Contrast error, as a percentage, does not change with N.
```

B.3 imagingScenario.m

```
% % Most detectors have SNR = 2 at about 2 nw/mm^2. We have exceeded
this
% % level by a factor of 4, which is not as much as I'd like.

% Options:
% - Relax the pixels per speckle sampling: feasible, 4
% - Reduce the propagation distance (use a smaller area per pixel): no
good
% - Increase source power: feasible but left as a last resort (more
% security paperwork)
% - Illuminate a smaller area (reduced speckle samples): feasible, 25
% speckles, 25*4^2 = 400 pixels

% For a Gaussian beam, the FWHM occurs at 0.5888 times the beam waist.
The
% power through that FWHM is given by P*(1 - exp(-2*(r/w)^2)) and is
% exactly half of the total power.

% Assume that 1.5 mw of illumination is distributed among 1600 pixels.
% Also, assume a perfectly lambertian surface.
Is = 0.0015/1600/pi;  % source intensity, w/sr

% Determine the energy entering the aperture per pixel
apDiam = 0.00272;
apArea = pi*(apDiam/2)^2;
dist = 2.934;
apFlux = Is*apArea/dist^2;  % power entering the aperture per pixel, w

% Determine the power density at the detector pixel
pixArea = (2*6.7e-6)^2;
pixIrrad = apFlux/pixArea;  % w/m^2

% Convert to w/mm^2 for comparison with the camera's minimum detectable
% irradiance:
pixIrrad_perMM = pixIrrad/1000^2;

timesMin = pixIrrad_perMM/(2e-9);
% Now, we are receiving about 30 times the minimum irradiance for
imaging.

% How many electrons are generated assuming 30% QE during a 0.001
second
% exposure?
pixelEnergy = apFlux*0.001;

h = 6.626*10^-34;
c = 2.998*10^8;
lambda = 670.96e-9;
QE = 0.3;

E = h*c/lambda;         % photon energy
photonCount = pixelEnergy/E;
electronCount = photonCount*QE;
```

Bibliography

Barakat, Richard. “First-order probability densities of laser speckle patterns observed through finite-size scanning apertures,” *Optica Acta*, **20**(9): 729-740, 1973.

Baribeau, Rejean and Marc Rioux. “Influence of speckle on laser range finders,” *Appl. Optics*, **30**(20): 2873-2878, 10 July 1991.

-----. “Centroid fluctuations of speckled targets,” *Appl. Optics*, **30**(26): 3752-3755, 10 September 1991.

Boeing Commercial Airplane Company. *Aircraft Surface Coatings Summary Report*. NASA Contractor Report 3661. Contracts NAS1-14742 and NAS1-15325. Seattle, Washington, January 1983.

Boeing Defense, Space & Security. *Directed Energy Systems (DES).* May 2014 http://www.boeing.com/assets/pdf/defense-space/ic/des/files/DES_overview.pdf.

Bures, Jacques, Claude Delisle, and Andrzej Zardecki. “Détermination de la Surface de Cohérence à Partir d'une Expérience de Photocomptage,” *Canadian Journal of Physics*, **50**(8): 760-768, 1972.

Butler, Amy. “Lights Out For The Airborne Laser,” *Aerospace Daily & Defense Report*. 21 December 2011 http://aviationweek.com/awin/lights-out-airborne-laser.

Chen, Chunyi, and Huamin Yang. “Temporal spectrum of beam wander for Gaussian Shell-model beams propagating in atmospheric turbulence with finite outer scale,” *Opt. Letters*, **38**(11), 1887-1889, 1 June 2013.

Cusumano, Salvatore J., Steven T. Fiorino, Richard J. Bartell, Matthew J. Krizo, William F. Bailey, Rebecca L. Beauchamp, Michael A. Marciniak. “Modeling bistatic spectral measurements of temporally evolving reflected and emitted energy from a distant and receding target,” *J. Appl. Remote Sens.*, 5: 053549, 2011.

Dabas, Alain, Pierre H. Flamant, Philippe Salamitou. “Characterization of pulsed coherent Doppler LIDAR with the speckle effect,” *Appl. Optics*, **33**(27): 6524-6532, 20 September 1994.

Dayton, David, Jeffrey Allen, Rudolph Nolasco, Gregory Fertig, and Michael Myers. “Comparison of fast correlation algorithms for target tracking,” *Proc. SPIE*, 8520: 85200G, 2012.

Deninger, Anselm, and Thomas Renner. *12 Orders of Coherence Control: Tailoring the coherence length of diode lasers*. Appl-1010. TOPTICA Photonics AG. Graefelfing, Germany, 3 August 2010.

Elbaum, M., M. Greenbaum, and M. King. "A wavelength diversity technique for reduction of speckle size," *Opt. Comm.*, **5**(3): 171-174, 1972.

Fiorino, Steven T., Robb M. Randall, Richard J. Bartell, John D. Haiducek, Mark F. Spencer, and Salvatore J. Cusumano. "Field Measurements and Comparisons to Simulations of High Energy Laser Propagation and Off-Axis Scatter," *Proc. SPIE*, 7814: 78140P, 2010.

Fitts, John M. "Precision correlation tracking via optimal weighting functions," *Proc. of the 18th IEEE Conference on Decision and Control including the Symposium on Adaptive Processes*, 280-283, 1979.

Godimetla, R., R. Holmes, and J. Riker. *Modeling of Partial Spatial and Temporal Coherence and Implications For Active Track And Active Imaging*. Technical Report. 23 September 2012.

Goodman, Joseph W. *Statistical Optics*. New York: John Wiley and Sons, 2000.

-----. *Speckle Phenomena in Optics: Theory and Applications*. Englewood, CO: Roberts and Company, 2007.

High Energy Laser Joint Technology Office. *Beam Control Technology State of the Art Assessment Report*. Albuquerque, New Mexico, 17 October 2013.

Holmes, Richard B. "Mean and variance of energy reflected from a diffuse object illuminated by radiation with partial temporal coherence," *J. Opt. Soc. Am. A*, **20**(7): 1194-1200, July 2003.

Hu, Yi-Qun. "Dependence of polychromatic-speckle-pattern contrast on imaging and illumination directions," *Appl. Optics*, **33**(13): 2707-2714, 1 May 1994.

Huntley, Jonathan M. "Simple model for image-plane polychromatic speckle contrast," *Appl. Optics*, **38**(11): 2212-2215, 10 April 1999.

Hyde IV, Milo W., Santasri Basu, Mark F. Spencer, Salvatore J. Cusumano, and Steven T. Fiorino. "Physical optics solution for the scattering of a partially-coherent wave from a statistically rough material surface," *Opt. Express*, **21**(6): 6807–6825, 2013.

Korotkova, O., L. C. Andrews, and R. L. Phillips. "Speckle propagation through atmospheric turbulence: effects of a random phase screen at the source," *Proc. SPIE*, 4821: 98–109, 2002.

-----. “Model for a partially coherent Gaussian beam in atmospheric turbulence with application in Lasercom,” *Opt. Eng.*, **43**(2): 330-341, 2004.

LaGrone, Sam. “U.S. Navy Allowed to Use Persian Gulf Laser for Defense,” USNI News. 10 December 2014 http://news.usni.org/2014/12/10/u-s-navy-allowed-use-persian-gulf-laser-defense.

Markhvida, Igor, Lioudmila Tchvialeva, Tim K. Lee, and Haishan Zeng. “Influence of geometry on polychromatic speckle contrast,” *J. Opt. Soc. Am. A*, **24**(1): 93-97, January 2007.

McKechnie, T. S. “Image-plane speckle in partially coherent illumination,” *Optical and Quantum Electronics*, 8: 61-67, 1976.

McManamon, Paul F. “Review of ladar : a historic, yet emerging, sensor technology with rich phenomenology,” *Opt. Eng.*, **51**(6): 060901, 2012.

Merritt, Paul H. *Beam Control for Laser Systems*. Directed Energy Professional Society, High Energy Laser Joint Technology Office, 2012.

Motes, R. Andrew and Richard W. Berdine. *Introduction to High-Power Fiber Lasers*. Albuquerque: Directed Energy Professional Society, 2009.

Nadarajah, Saralees. “A Review of Results on Sums of Random Variables,” *Acta Appl. Math.*, **103**(2): 131-140, 6 March 2008.

Nakagawa, K. and T. Asakura. “Average contrast of white-light image speckle patterns,” *Optica Acta*, **26**(8): 951-960, 1979.

Negro, J., R. Brunsen, D. Dean, J. Kann, and E. Duff. “A System Engineering Approach for Active Track Jitter Performance Evaluation,” *J. Directed Energy*, **4**(2): 147, 2010.

Nelson, Douglas H. and others. “Wave optics simulation of atmospheric turbulence and reflective speckle effects in CO2 lidar,” *Appl. Optics*, **39**(12): 1857-1871, 20 April 2000.

Parry, G. “Speckle Patterns in Partially Coherent Light,” in *Laser Speckle and Related Phenomena*. Berlin: Springer-Verlag, 1975.

Pederson, H. M. “On the contrast of polychromatic speckle patterns and its dependence on surface roughness,” *Optica Acta*, **22**(1): 15-24, 1975a.

-----. “Second-order statistics of light diffracted from Gaussian, rough surfaces with applications to the roughness dependence of speckle,” *Optica Acta*, **22**(6): 523-535, 1975b.

Post, Stephen G. “High average power diode-pumped solid-state laser illuminators for HEL beam control,” *Proc. SPIE*, 5414: 85-100, 2004.

Praus II, Robert W., Keith Beardmore, Boris P. Venet. *The “Light Tunneling” Optical Propagation Method in WaveTrain*. Technical Memorandum. MZA Associates Corporation, 20 November 2007.

Riker, J. F., G. A. Crockett, and R. L. Brunson. “The time-domain analysis simulation for advanced tracking (TASAT),” *Proc. SPIE*, 1697: 297-309, 1992.

Riker, Jim and others. “Active tracking with moderate power lasers,” *Proc. SPIE*, 5552: 123-132, 2004.

Riker, Jim F. “Active tracking lasers for precision target stabilization,” *Proc. SPIE*, 5087: 1-12, 2003.

-----. “Results from precision tracking tests against distant objects,” *Proc. SPIE*, 6569: 65690H, 2007.

-----. “Requirements on active (laser) tracking and imaging from a technology perspective,” *Proc. SPIE*, 8052: 805202, 25 April 2011.

Rodrigues, Carlos M. P. and Joao L. Pinto. “Contrast of polychromatic speckle patterns and its dependence to surface heights distribution,” *Opt. Eng.*, **42**(6): 1699-1703, June 2003.

Rotge, J., D. Christensen, A. Klemas, G. Loos, and D. Merriman. “Laser diode coherence length variation with drive current: a tool for dispersion measurements,” *Proc. SPIE*, 1625: 350-358, 1992.

Sprague, Robert A. “Surface roughness measurement using white light speckle,” *Appl. Optics*, **11**(12): 2811-2816, 1972.

Stanton, Brian, William Coburn, and Thomas J. Pizzillo. *Armor Plate Surface Roughness Measurements*. ARL-TR-3498, Adelphi, MD: Army Research Laboratory, April 2005.

Steinvall, Ove, Tomas Chevalier, Pierre Andersson, and Magnus Elmqvist. “Performance modeling and simulation of range-gated imaging systems,” *Proc. SPIE*, 6542: 654218, April 2007.

St. Pierre, Randall J. and others. “Active Tracker Laser (ATLAS),” *IEEE J. Sel. Top. Quant. Electron*, **3**(1): 64-70, February 1997.

Tchvialeva, Lioudmila, Tim K. Lee, Igor Markhvida, David I. McLean, Harvey Lui, and Haishan Zeng. “Using a zone model to incorporate the influence of geometry on polychromatic speckle contrast,” *Opt. Eng.*, **47**(7): 074201, July 2008.

Tchvialeva, Lioudmila, Igor Markhvida, Tim K. Lee. “Error analysis for polychromatic speckle contrast measurements,” *Optics and Lasers in Engineering*, **49**: 1397-1401, 2011.

Teng, Shu-Yun, Chuan-Fu Cheng, Man Liu, Li-Ren Liu, and Zhi-Zhan Xu. “Properties of Movement and Boiling of Speckles Produced by Moving Objects Illuminated with Partially Coherent Light,” *Chinese Phys. Lett.*, **20**(1): 68–71, 2003.

Thorlabs. “CMOS Cameras: USB 2.0 and USB 3.0 Specs.” Unpublished measurements. n. pag. http://www.thorlabs.com/newgrouppage9.cfm?objectgroup_id=4024. Accessed 13 December 2014.

Van Zandt, Noah R., Salvatore J. Cusumano, Richard J. Bartell, Santasri Basu, Jack E. McCrae, and Steven T. Fiorino. “Comparison of coherent and incoherent laser beam combination for tactical engagements,” *Opt. Eng.*, **51**(10), 10 October 2012.

Van Zandt, Noah R., Steven T. Fiorino, Jack E. McCrae, Nathan P. Wurst. “Speckle Effects for Aimpoint Identification in Tactical Active Tracking Engagements,” Presented at DEPS Annual Symposium, Huntsville, Alabama, 13 March 2014.

Wong, Sebastian. “Advanced Correlation Tracking of Objects in Cluttered Imagery,” *Proc. SPIE*, 5810: 158-169, 2005.

List of Symbols, Abbreviations, and Acronyms

BRDF – bidirectional reflectance distribution function, a measure of the directionality of a material's reflection

CMOS – complimentary metal-oxide semiconductor, a common type of optical detector

CRAM – counter rocket, artillery, and mortar

DE – directed energy

FWHM – full width half maximum value

HEL – high energy laser

IFOV – instantaneous field of view, which in this work is always used to refer to the instantaneous field of view of a single pixel

LED – light emitting diode

LOS – line of sight

LWIR – long-wave infrared, sometimes defined as the 8 to 12 μm spectral window

MWIR – mid-wave infrared, sometimes defined as the 3 to 5 μm spectral window

PDF – probability density function

PMT – photomultiplier tube, a non-imaging optical detector known for exceptional dynamic range and signal to noise ratio

PSF – point spread function

RHA – rolled homogeneous armor

SEM – standard error of the mean, an approximation for the error bound of the computed mean value for Gaussian-distributed error

SNR – signal-to-noise ratio

TEC – thermoelectric cooler

UAV – unmanned aerial vehicle

REPORT DOCUMENTATION PAGE		*Form Approved* *OMB No. 0704–0188*

1. REPORT DATE (DD–MM–YYYY)	2. REPORT TYPE	3. DATES COVERED *(From — To)*
26-03-2015	Master's Thesis	October 2012 to March 2015

4. TITLE AND SUBTITLE	5a. CONTRACT NUMBER
Modeled and Measured Partially Coherent Illumination Speckle Effects From Sloped Surfaces For Tactical Tracking	n/a
	5b. GRANT NUMBER n/a
	5c. PROGRAM ELEMENT NUMBER n/a
6. AUTHOR(S) Van Zandt, Noah R., Civilian, USAF	5d. PROJECT NUMBER n/a
	5e. TASK NUMBER n/a
	5f. WORK UNIT NUMBER n/a
7. PERFORMING ORGANIZATION NAME(S) AND ADDRESS(ES) Air Force Institute of Technology Graduate School of Engineering and Management (AFIT/EN) 2950 Hobson Way Wright-Patterson AFB OH 45433-7765	8. PERFORMING ORGANIZATION REPORT NUMBER AFIT-ENP-MS-15-M-257
9. SPONSORING / MONITORING AGENCY NAME(S) AND ADDRESS(ES) High Energy Laser Joint Technology Office 801 University Blvd SE Ste. 209 Albuquerque, NM 87106 (505) 248-8209 Tisha.Mangold.ctr@jto.hpc.mil	10. SPONSOR/MONITOR'S ACRONYM(S) HEL-JTO
	11. SPONSOR/MONITOR'S REPORT NUMBER(S) n/a

12. DISTRIBUTION / AVAILABILITY STATEMENT
DISTRIBUTION STATEMENT A. Approved for public release; distribution is unlimited.

13. SUPPLEMENTARY NOTES
This work is declared a work of the U.S. Government and is not subject to copyright protection in the United States.

14. ABSTRACT
The statistical properties of speckle relevant to short to medium range (tactical) active tracking involving polychromatic (partially temporally coherent) illumination are investigated. A numerical model is developed to allow rapid simulation of speckled images including the speckle contrast reduction effects of illuminator bandwidth, surface slope and roughness, and the polarization properties of both the source and the reflection. Regarding surface slope, Huntley's theory for speckle contrast, which employs geometrical approximations to decrease computation time, is modified to increase accuracy by incorporation of a geometrical correction factor and better treatment of roughness and polarization. The resulting model shows excellent agreement with more exact theory over a wide range. An experiment is conducted to validate both the numerical model developed here and existing theory. A short coherence length diode laser source is reflected off of a silver-coated diffuse surface. Speckle data is gathered for 16 surface slope angles corresponding to speckle contrast between about 0.55 and 1. Taking Hu's theory as truth, the measurements have -1.1% mean difference with 2.9% standard deviation, while the modified Huntley equation has 1.4% mean difference with 1.0% standard deviation. Thus, the theory is validated over the range of this experiment.

15. SUBJECT TERMS
active illumination, polychromatic speckle, sloped surface speckle, speckle contrast, tactical tracking

16. SECURITY CLASSIFICATION OF:			17. LIMITATION OF ABSTRACT	18. NUMBER OF PAGES	19a. NAME OF RESPONSIBLE PERSON
a. REPORT U	b. ABSTRACT U	c. THIS PAGE U	UU	104	Dr. Steven T. Fiorino, AFIT/ENP
					19b. TELEPHONE NUMBER (Include Area Code) (937) 255–3636 x 4506 steven.fiorino@afit.edu

Standard Form 298 (Rev. 8–98)
Prescribed by ANSI Std. Z39.18